remote sensing

MDPI

Review

A Tropical Cyclone or Typhoon as an Element of the Earth–Atmosphere–Ionosphere–Magnetosphere System: Theory, Simulations, and Observations

Leonid F. Chernogor

Department of Space Radio Physics, V. N. Karazin Kharkiv National University, 61022 Kharkiv, Ukraine; leonid.f.chernogor@gmail.com

Abstract: The premise has been validated that a tropical cyclone (TC, typhoon, hurricane), one of the most powerful large-scale formations systematically arising in the atmosphere, is an element of the ocean–atmosphere–ionosphere–magnetosphere system. The TC plays a crucial role with regard to a global-scale mass and energy exchange in this system. The study of this system encompasses a broad spectrum of physical phenomena occurring and processes operating within the system components, as well as the mechanisms of their interactions. The problem under discussion pertains to interdisciplinary science. Its scope ranges from different Earth sciences to geospace sciences, which comprise the physics of the ocean, meteorology, the physics of the Earth's atmospheric and space environment, etc. Observations of the ionospheric response to the impact of a number of unique typhoons made using multifrequency multiple path oblique incidence ionospheric sounding have confirmed the definitive role that the internal gravity waves and infrasound play in producing atmospheric–ionospheric disturbances. It has been demonstrated that these disturbances are capable of significantly affecting the characteristics of high-frequency radio waves.

Keywords: system analysis; tropical cyclone (typhoon); typhoon parameters; typhoon models; typhoon action mechanisms; acoustic–gravity waves; electric effects; magnetic effects; electromagnetic effects; observations

Citation: Chernogor, L.F. A Tropical Cyclone or Typhoon as an Element of the Earth–Atmosphere–Ionosphere–Magnetosphere System: Theory, Simulations, and Observations. *Remote Sens.* **2023**, *15*, 4919. https://doi.org/10.3390/rs15204919

Academic Editors: Yuriy G. Rapoport, Volodymyr Grimalsky, Anatoly Kotsarenko and Gianfranco Cianchini

Received: 16 August 2023
Revised: 6 October 2023
Accepted: 8 October 2023
Published: 11 October 2023

1. Introduction

In recent decades, it has become clear that processes operating on the surface of the Earth, over the Earth's surface, and in near geospace are treated best within the systems paradigm [1–4]. It is important that the Earth (inner shells)–atmosphere–ionosphere–magnetosphere formation is an open dynamical and nonlinear system. The properties of this system manifest themselves well under the action of powerful sources releasing energy (see, e.g., [2–4]). The coupling between the system components is through acoustic–gravity waves (an AGW mechanism), electromagnetic emissions (an electrodynamic mechanism), and quasi-steady electric fields (an electrical mechanism). The powerful localized sources of energy act to launch a myriad of large- and even global-scale processes in the system. These include the generation and propagation of wave disturbances, the generation of geophysical fields and instabilities, lightning-induced electron precipitation, enhancements in radio noise, etc. Attempts have been made to develop elements of a model for ionospheric disturbances and for variations in ionospheric electric fields due to enhancements in ionization, and electrophysical, chemical, and meteorological processes in the troposphere.

The results of satellite (orbit altitude of $z \approx 950$ km) measurements of quasi-steady electric field variations over the areas where the formation and intensification of TCs occur are presented in [5,6]. The TCs turn out to be the generators of bipolar changes in an electric field of 10–20 mV/m. The satellite measurements show the duration of this process to be about 2–3 min, thereby suggesting a disturbed ionospheric region with horizontal extents of (1–1.5) $\times 10^3$ km. A tropical cyclone is generally considered to be formed once the mean

surface winds attain a hurricane force in excess of 35 m/s on the Beaufort wind force scale. A tropical cyclone that occurs in the northwestern Pacific Ocean is termed a typhoon.

The results obtained in [5–13] permit us to consider a TC (typhoon) to be one of the elements of the ocean–atmosphere–ionosphere–magnetosphere system, which couples the system components listed above. The elucidation of the TC (typhoon) manifestations in the upper atmosphere and geospace has contributed to the understanding of basic processes operating in the system, which is of scientific significance for the studies of the TC (typhoon) as an element of the specified system.

The study of the response of the ionosphere and magnetosphere to the formation and evolution of a TC (typhoon) is also of great practical importance because the kinetic energy of an average typhoon exceeds the energy of the greatest earthquakes or the most violent volcanic eruptions [14–16]. Typhoons are the most destructive large-scale atmospheric formations on our planet. Hurricanes and typhoons are known to have wind speeds exceeding 90 m/s and radii of gale wind attaining 750 km. The pressure deficit at the center of a typhoon sometimes approaches 140 hPa. The kinetic energy of strong hurricanes and typhoons exceeds 10^{18} J. In addition, the rate of occurrence of intense typhoons continuously increased during the past decades [5], posing a greater danger to humans. Therefore, the creation of a reliable satellite network monitoring TCs is a pressing problem. The solution to this problem requires a thorough study of an entire chain of processes, from all factors affecting tropical cyclone formation (cyclogenesis) to the impact of TCs and typhoons on the parameters of the atmosphere, ionosphere, and magnetosphere, along with the development of models for all relevant processes.

The influence of meteorological processes, namely, tropical cyclones, on the ionosphere was identified for the first time in [17]. The observations of traveling ionospheric disturbances (TIDs) as the manifestations of the atmospheric gravity waves (AGWs) generated by hurricanes were described in [18]. The influence of infrasound generated by thunderstorms was studied in [19]. Observations of AGWs of meteorological origin have been reported elsewhere [20–22].

The coupling between typhoons and the ionosphere and the overlying magnetosphere occurs via a range of mechanisms. Observational studies conducted in recent years have shown that typhoons significantly influence the upper atmosphere, including the ionosphere. Recently, theoretical studies on the coupling between the lower and upper atmosphere, which occurs through AGWs, have been published as well [23–27]. Such a mechanism for coupling is naturally termed the acoustic–gravity mechanism [1,3,4].

Typhoons are accompanied by water vapor condensation, the development of a powerful convective lift, and the appearance of severe thunderstorms [28,29]. Lightning discharges act to generate electromagnetic emissions that may be capable of heating electrons and perturbing the electron density in the ionospheric *D*-region [1,3,4,30]. The points are as follows. Large enough fluxes of electromagnetic emissions in the 1–100 kHz frequency range lead to pitch-angle scattering of energetic electrons in the radiation belts via wave–particle interaction, and consequently, part of the electron precipitates into the lower ionosphere [31–33]. As a result, secondary perturbations in the plasma conductivity (~100–150 km altitude) and in the geomagnetic and electric fields capable of affecting processes in the magnetosphere can arise. Such a mechanism should be considered as an electromagnetic mechanism [1,3,4].

An increase in the quasi-steady electric field may be of different origin [28,32–35]. Localized ~10^{-9}–10^{-8} A m^{-2} electric currents arise within thunderstorm clouds at 10–15 km altitude, which disturbs the global electric circuit and increases by 1–2 orders of magnitude quasi-sinusoidal electric fields that are mapped to the ionosphere and magnetosphere and affect the motion of high-energy electrons trapped in the radiation belts. Under certain conditions, the precipitation of these electrons into the ionosphere may occur, and a repeated coupling between the subsystems in the ocean–atmosphere–ionosphere–magnetosphere (OAIM) system happens [1,3,4]. This mechanism for coupling may be

termed the electrical mechanism [1,3,4]. Thus, powerful typhoons are capable of governing the coupling between the subsystems in the OAIM system.

A lot of studies deal with the acoustic–gravity mechanism; therefore, this mechanism has been studied better than the others. The major role the AGWs play in coupling different atmospheric regions under the influence of typhoons and hurricanes to the upper atmosphere is discussed in [36–49]. For probing the ionosphere, these researchers invoked measurement techniques that include GPS technology, ionosondes, rocket techniques, and the high-frequency (HF) Doppler technique.

The manifestations of the ionospheric response to the super typhoons Hagibis, Ling-Ling, Faxai, Lekima, and Kong-Rey in radio wave characteristics in the 5–10 MHz band have been studied in [10–13]. The variations in the main features of radio waves have been determined, and aperiodic and quasi-sinusoidal perturbations in the electron density have been ascertained.

The effect of sudden stratospheric warming events, variations in space weather, solar activity, and AGWs on the coupling between the subsystems in the atmosphere–ionosphere system has been analyzed in the review [50], whereas twenty years earlier, the review by [51] could only point to the AGW/TID relationship. Since then, data have been compiled on some parameters of medium-scale traveling ionospheric disturbances (MSTIDs), one of the mechanisms for affecting the ionosphere by typhoons. The parameters of interest to typhoon/ionosphere coupling studies include the propagation direction. Of particular interest to the current study, which is conducted in the area roughly to the west of Japan, are data collected in Japan. Using airglow images, a clear preference for southwestward propagation has been shown by [52,53]. Observations made over a seven-year period in Indonesia estimated the propagation direction to be within ± 30 degrees from the source directions of MSTIDs in 81% of the MSTID events [54]. Observations made in the western hemisphere are in agreement with those made over the Pacific Ocean [55–57]. The latter study is noteworthy because it showed that the observed anisotropy in the propagation direction can be fully explained by the filtering process of the wind.

The results of the latest observations are presented in papers [10,11,42,43,48,58–66]. They show that the influence of typhoons on the ionosphere might be expected to be significantly dependent on typhoon parameters, local time, season, solar cycle changes, and the state of atmospheric and space weather. To date, there remains insufficient knowledge about these influences, and therefore, the study of the ionospheric response to any new typhoon is of interest.

The purpose of this work is to describe, for the first time, a developed and schematic model for TCs (typhoons) and the basic processes operating in the ocean–atmosphere–ionosphere–magnetosphere system, to discuss the mechanisms of the system component couplings, to estimate the accompanying effects, and to present examples of the impact that unique typhoons have on the ionosphere and the characteristics of HF radio waves.

The paper is structured as follows. First, geometric, hydrodynamic, and thermodynamic parameters of TCs are characterized. Next, energetics estimates are presented. This is followed by a schematic description of the mechanisms coupling the system components in the ocean–atmosphere–ionosphere–magnetosphere system, and the estimates of the respective parameters and effects are given. Then, examples of the observations of ionospheric responses to the impacts of unique typhoons and illustrations of the variations in the characteristics of HF radio waves are provided. Finally, the main results of the work are summarized in the Conclusions Section.

2. Geometric Parameters of Tropical Cyclones (Typhoons)

TCs (typhoons) are complicated objects to model. Until recently, repeatable attempts have been made to develop empirical, analytical, and computer models (see, e.g., Refs. [67–72]). The simplest and, at the same time, adequate model is an analytical model of TCs (typhoons) developed by V.V. Shuleikin [72], which is used in this work. The model assumes that the trajectories of air particles are logarithmic spirals.

Each TC (typhoon) has an internal boundary of radius r_0. Inside this circular formation, termed the eye, the wind speed is close to zero, whereas it attains a maximum value of V_0 at the distance $r = r_0$ from the center of the eye, and further to the periphery, it decreases and tends to zero at the TC external boundary of radius R_0. Within a TC (typhoon), it makes sense to single out the core of a cyclone with a radius varying from r_0 to r_1. Within the core, the vertical component of the velocity of air particles w is positive, whereas $w < 0$ within the ring $R_0 > r > r_1$. The core can be defined by other properties describing a particular physical process (see below).

A TC (typhoon) occupies the entire troposphere in height (about 20 km), with a scale height of $H \approx 8$ km. The magnitude of the velocity vector **V** within a typical TC (typhoon) is usually a maximum at the altitude of $h_0 \approx 500$ m. The angle χ between the velocity vector and its tangential component in the spiral v is close to 18°.

Table 1 shows the values of the geometric parameters listed above for a typical typhoon of average intensity.

Table 1. Geometric and mass characteristics of a typical typhoon.

Shape	close to a spiral
Eye radius	$r_0 = 15$ km
Core radius for $w(r_1) = 0$	$r_1 = R_0/e = 225$ km
External radius	$R_0 = 600$ km
Effective radius of water vapor condensation zone	$r_2 = \alpha r_1 - r_0 \approx 46$ km
Thickness	$h \approx 15$–20 km
Horizontal speed peak height	$h_0 = 500$ m
Air mass	$m = 1.2 \times 10^{16}$ kg
Air mass in core	$m(r_1) = 2 \times 10^{15}$ kg
Effective mass	$m_{ef} \approx 6.9 \times 10^{14}$ kg
Surface area of water vapor condensation zone	$S_c \approx 1.6 \times 10^{11}$ m^2

The geometric parameters of TCs (typhoons) determine the air mass involved in motion, as given by

$$m = \rho \pi R_0^2 H$$

where $\rho \approx \rho_0 \approx 1.3$ kg/m^3 is the air density at an altitude of $z = 0$. Typical values for air masses in the typhoon and its core are 10^{16} kg and 10^{15} kg, respectively.

3. Hydrodynamic Parameters of Tropical Cyclones (Typhoons)

The tangential v and radial u components of the wind velocity vector within TCs (typhoons) are obtained from the Navier–Stokes equations given by [72]:

$$\frac{1}{\rho}\frac{\partial p}{\partial r} = 2\omega v + \frac{v^2}{r} + \nu_z \frac{\partial^2 u}{\partial z^2} \quad (1)$$

$$\frac{1}{\rho}\frac{\partial p}{r\partial \psi} = 2\omega u + \frac{u\nu}{r} + \nu_r \frac{\partial^2 v}{\partial r^2} + \nu_z \frac{\partial^2 v}{\partial z^2} \quad (2)$$

where p and ρ are the air pressure and mass density, φ and ψ are the latitude and azimuth of the observation site, $\omega = \omega_0 \sin \varphi$, ω_0 is the Earth's angular velocity, and ν_z and ν_r are the coefficients of the kinematic viscosity taking into account friction between the horizontal air layers and lateral friction, respectively.

It is often possible to neglect the viscosity in Equation (1). In addition, if the asymmetry in the TC is neglected, i.e., $\partial/\partial\psi = 0$, then the system of equations is simplified as follows:

$$\frac{1}{\rho}\frac{\partial p}{\partial r} = 2\omega v + \frac{v^2}{r} \tag{3}$$

$$0 = 2\omega u + \frac{u\nu}{r} + \nu_r\frac{\partial^2 v}{\partial r^2} + \nu_z\frac{\partial^2 v}{\partial z^2} \tag{4}$$

Given the distribution $p(r)$, the dependences $v(r)$ and $u(r)$ could be found from Equations (3) and (4). However, the coefficients ν_r and ν_z are generally unknown. Therefore, it has been a common practice to follow another way. First, the functional dependences $v(r)$ and $u(r)$ are determined from the observational data, then the dependence $p(r)$ is calculated, and finally the ν_r and ν_z dependences are estimated.

The observational data were fitted with the following analytic expression for the tangential component of the velocity at the altitude level h_0, at which $\partial v/\partial z = \partial u/\partial z = 0$ [72]:

$$v(r) = v_0(1 - \alpha \ln r/r_0) \tag{5}$$

Here $v_0 = v(r_0)$, $\alpha^{-1} = \ln R_0/r_0$, usually $\alpha \approx 0.27$. Further, it will be assumed that cyclones have a similarity property, and $\alpha \approx 0.27$ is true for TCs of different sizes.

If the angle χ is assumed to be constant within a particular TC, then the projection u at the altitude level h_0 is governed by the relation analogous to that in Equation (5):

$$u = u_0(1 - \alpha \ln r/r_0),\ u_0 = v_0 \mathrm{tg}\chi. \tag{6}$$

Consequently, the magnitude of the velocity vector at the altitude level h_0 is equal to $V = v \sec \chi$.

The relation for the vertical component of the wind velocity in TC (typhoon) can be obtained by making use of Equation (6) and the continuity equation expressed in the form [72].

$$w = \frac{h_0}{r}\frac{\partial}{\partial r}(ur) \tag{7}$$

Substituting Equation (6) in Equation (7) yields

$$w = \frac{h_0}{r}(u - \alpha u_0) = \frac{h_0}{r}u_0(1 - \alpha - \alpha \ln \frac{r}{r_0}) \tag{8}$$

In particular,

$$w_0 = w(r_0) = \frac{h_0}{r_0}u_0(1 - \alpha) \tag{9}$$

The relation in Equation (8) is used to find the distance r_1 where $w(r) = 0$, which turns out to be $r_1 = R_0/e$, where e is the base of the natural logarithm.

Substituting Equation (5) in Equation (3) gives

$$\frac{1}{\rho}\frac{\partial p}{\partial r} = 2\omega v_0(1 - \alpha \ln r/r_0) + \frac{v_0^2}{r}(1 - \alpha \ln r/r_0)^2. \tag{10}$$

Integrating Equation (10) yields

$$p(r) = p_0 + 2\omega\rho v_0[\alpha(R_0 - r) + r(\alpha_r - 1)] + \frac{\rho v_0^2}{3\alpha}(1 - \alpha_r^3)$$

where $\alpha_r = \alpha \ln r/r_0$, p_0 is the undisturbed pressure, and $\rho \approx \rho_0$. The pressure deficit at the internal boundary of TC (typhoon), i.e., at $r = r_0$ is given by

$$\Delta p(r_0) = p_0 - p(r_0) = -2\omega\rho v_0[\alpha(R_0 - r_0) - r_0] - \frac{\rho v_0^2}{3\alpha}. \quad (11)$$

If the first term on the right-hand side of Equation (11) is significantly less than the second term, then

$$\Delta p(r_0) \approx -\frac{\rho v_0^2}{3\alpha} = -\frac{\rho v_0^2}{3} \ln \frac{R_0}{r_0}. \quad (12)$$

The dependence of the typhoon pressure deficit on the typhoon size and velocity v_0, which is estimated with the relation Equation (11), is presented in Table 2, which shows that the magnitude of the pressure deficit is weakly dependent on R_0 and is determined mainly by the velocity v_0.

Table 2. Typhoon pressure maximum deficit (in hPa) vs. velocity v_0 (m/s) and typhoon size.

	v_0 **(m/s)**						
R_0 **(km)**	**40**	**50**	**60**	**70**	**80**	**90**	**100**
300	−29.2	−44	−61.8	−82.6	−106	−133	−163
450	−31.6	−47	−65.4	−86.8	−111	−139	−169
600	−35	−50	−69.5	−91.6	−117	−144	−176
750	−37	−54	−74	−97	−122	−152	−180

Representative values for the main hydrodynamic parameters of a typical TC (typhoon) are given in Table 3.

Table 3. Hydrodynamic parameters of a typical typhoon.

Air pressure deficit maximum	$\Delta p(r_0)$ = 120 hPa
Air density	$\rho \approx$ 1.2–1.3 kg/m^3
Tangential speed	$v_0 = v(r_0, h_0)$ = 60 m/s $v_{00} = v(r_0, 0) = k_3 v_0$
Radial speed	$u_0 = u(r_0, h_0) = v_0 \tan \chi$ = 20 m/s $u_{00} = u(r_0, 0) = k_3\ u_0$
Total horizontal speed	$V_0 = V(r_0, h_0) = v_0 \sec \chi$ = 63 m/s $V_{00} = V_0(r_0, 0) = k_3\ V_0$
Vertical speed	$w_0 = w(r_0, h_0) = \frac{h_0}{r_0} u_0(1 - \alpha)$ = 0.5 m/s
Velocity of translational motion	v_1 = 5–10 m/s
Length of movement	$L \approx$ 3000–5000 km
Angle between the velocity vector and its tangential component	$\chi = 18^\circ$
Centripetal acceleration maximum value	$\frac{v_{00}^2}{r_0} \approx 19.44 \times 10^{-2}$ m/s^2
Coriolis acceleration maximum value	$2v_{00}\ \omega_0 \sin \varphi \approx 5.5 \times 10^{-3}$ m/s^2, $\varphi = 45^\circ$

4. General Information on Couplings in the Ocean–Land–Atmosphere Subsystem

A TC (typhoon), as well as other meteorological phenomena, is formed as a result of coupling between the constituent components of the ocean–land–atmosphere (OLA) subsystem. The OLA subsystem is generally characterized by self-excitation processes, and a typhoon is one of the most powerful such phenomena. Tropical cyclones have their origins in the intertropical convergence zone where the warm oceanic surface (sea critical temperature of $t_c \approx 26.5\ ^\circ$C) heats the air that rises in parcels, which can, under specific conditions, cause large clusters of thunderstorms to funnel the warm moist air upward. The Coriolis force causes cyclonic rotation resulting in the formation of the low-pressure center.

The ocean, or rather its upper layers of thickness $h_1 \approx 10$–100 m, gives off its heat to heating air and to evaporating oceanic water, resulting in an increase in the kinetic energy. Rising, water vapor condenses and gives off heat to the air in the cyclone. If the water temperature t_1 becomes less than the air temperature, the air begins to heat the surface layer of the ocean, and consequently, a damped oscillatory process arises, which will be further described by the angular frequency ω_1 and the damping constant γ.

The air speed in a TC (typhoon) increases due to heat consumption from the surface layer of the oceanic water, whereas it decreases because of friction between the TC air and the oceanic surface. It is important that the friction force is proportional to the TC wind speed squared v^2.

The oceanic surface layer water cools, cold water upwelling occurs, and its mixing with warm water near the surface takes place. The steady water temperature t_f in the surface layer is determined by the balance of heat of solar origin. Tropical cyclones usually persist at temperatures of $t_f \approx 27$–30 °C. It should be noted that the intensity of upwelling is determined by the level of friction in the turbulent flow, which is proportional to v^2. Thus, the equation for the heat flow in the oceanic surface layer and the equation for the kinetic energy of the air rotational motion are both expected to be nonlinear. This means that both the OLA system and the processes operating in it are nonlinear.

5. Energetics of the Ocean–Atmosphere Subsystem

5.1. Oceanic Heat Loss

The total loss of the oceanic heat consists of two components: the losses through the surface area S_{11} occupied by the TC core and the losses through the surface area S_{12} of the TC track. The loss of internal energy dP_{T11} of the ocean through the differential area $dS_{11} = 2\pi r dr$ per unit time is given by

$$dP_{T11} = 2\pi \frac{h_1}{h} c_1 \rho_1 \Delta T_1 w(r) r dr, \tag{13}$$

where $c_1 = 4.2 \times 10^3$ J/(kg·K) and ρ_1 are the specific heat and density of water, respectively, ΔT_1 is the difference between the temperatures prior to and after the cyclone passage, h_1 is the maximum oceanic depth to which the cyclone cools water, and h is the altitude of the upper TC boundary (usually $h \approx 15$–20 km). In performing the integral of Equation (13) over the TC core radius, it is convenient to replace the dependence $\Delta T_1(r)$ by some mean value $\overline{\Delta T_1}$. Integrating Equation (13) yields

$$P_{T11} = c_1 \rho_1 \overline{\Delta T_1} \frac{h_1}{h} w_0 S_{11} \tag{14}$$

where $S_{11} = \frac{2\alpha}{(1-\alpha)e} \frac{r_0}{R_0} \pi R_0^2 \equiv k_{11}^2 S_0$, $S_0 = \pi R_0^2$, $w_0 = (1-\alpha) h_0 u_0 / r_0$. Then, Equation (14) shows that heat flows through the surface area S_{11}. The radius of the TC thermal core is given by $R_{11} = k_{11} R_0$, where $k_{11} = \left(\frac{2\alpha}{(1-\alpha)e} \frac{r_0}{R_0} \right)^{1/2} \approx 1/12$. In addition, $S_{11} \ll S_0$.

It should be noted that in calculating the power $P_{11,}$ the characteristic time constant Δt_h is assumed to be the time interval the air parcel takes to rise to the upper TC boundary, i.e., $\Delta t_h = h/w$.

Given the calculated magnitude of R_{11}, the differential dS_{12} may be expressed as $dS_{12} = 2R_{11} v_1 dt$. Then, the loss of the internal energy of the ocean to the moving cyclone per unit time is given by

$$P_{T12} = 2 c_1 \rho_1 \overline{\Delta T_1} h_1 R_{11} v_1.$$

The total power is equal to

$$PcTRhw_{T1} = P_{T11} + P_{T12} = c_1 \rho_1 \overline{\Delta T_1} R_{11} h_1 \left(\frac{\pi R_{11} w_0}{h} + 2 v_1 \right) \tag{15}$$

or

$$P_{T1} = c_1 \rho_1 \overline{\Delta T_1} R_0 h_1 \left(\frac{h_0}{h} k_v v_0 + 2 k_{11} v_1 \right) \quad (16)$$

where $k_v = \frac{2\pi\alpha}{e} \mathrm{tg}\chi$.

The power P_{T1} is spent on evaporating water and heating air. Given the air temperature of $t_2 \approx 25$ °C in a developing cyclone, the ratio, β_0, of the corresponding powers is approximately 3:1, i.e., $P_{T2} \approx (3/4)P_{T1}$ and $P_{T3} \approx (1/4)P_{T1}$ [70].

The loss of the internal energy during the lifetime of 6 days for a typical TC is close to 10^{21} J. This energy exceeds the energy of the greatest earthquake or the heat energy of the most powerful volcano by more than two orders of magnitude [15].

5.2. TC Kinetic Energy

An increase in the kinetic energy, E_{k1}, of the TC rotational motion leads to an increase in its angular momentum dK, i.e., $dE_{k1} \approx \omega_v dK$, where ω_v is the angular speed of the air in the TC. Here, $d\mathbf{K} = \mathbf{r} \times \mathbf{v}\, dm$ and its magnitude $dK = rv\, dm$. Since $dm = 2\pi\rho H r dr$, then $\omega_v r = v$,

$$E_{k1} = 2\pi \int_{r_0}^{R} \rho H v^2 r dr. \quad (17)$$

To exclude the altitude dependence, it is advisable to have v^2 averaged over height, i.e., to replace v^2 with $\overline{v^2} = k_1 v^2(h_0) \equiv k_1 v_0^2$. The coefficient $k_1 \approx 0.8$ has been determined from observational data [72]. Taking into account Equation (5) and performing the integral of Equation (17) yields

$$E_{k1} = \frac{1}{2} m_{ef} v_0^2, \; m_{ef} = k_1 \alpha^2 m. \quad (18)$$

At $\alpha \approx 0.27$, the value of $k_1 \alpha^2 \approx 5.8 \times 10^{-2}$, i.e., $m_{ef} << m$. This inequality reflects the fact that v abates with distance from the center of the cyclone.

For instance, at $R_0 = 600$ km, $H = 8$ km, $v_0 = 75$ m/s, we have $m = 1.2 \times 10^{16}$ kg, $m_{ef} \approx 6.9 \times 10^{14}$ kg, $E_{k1} \approx 2 \times 10^{18}$ J (see Tables 1 and 4).

It is important that the kinetic energy E_{k2} of the translational motion of TCs is somewhat smaller than E_{k1} because $v_1 << v_0$, but $m >> m_{ef}$. At $v_1 = 10$ m/s, we have $E_{k2} = mv_1^2/2 \approx 0.6 \times 10^{18}$ J $\approx 0.3\, E_{k1}$.

The total kinetic energy of TCs $E_k = E_{k1} + E_{k2}$ may exceed the energy of the greatest earthquake or volcano, which is of the order of 10^{18} J [15].

5.3. Power of Water Vapor Condensation

Within a cyclone at rest, the amount of heat released in the condensation of water vapor and carried upward within a ring of radius r and of width of dr per unit time is given by the expression

$$dP_c = 2\pi\lambda\rho_2 w r dr \quad (19)$$

where $\lambda = 2.26 \times 10^6$ J/kg is the specific heat of condensation and ρ_2 is the density of water vapor. Taking into account Equation (8) and integrating Equation (19), we obtain

$$P_c(ru_1) = 2\pi h_0 \lambda \rho_2 r_2 u_0 = 2\pi h_0 \lambda \rho_2 r_2 v_0 \mathrm{tg}\chi \quad (20)$$

where $r_2 = \alpha r_1 - r_0$. At $v_0 = 60$ m/s, $r_0 = 15$ km, $r_1 = 225$ km, and the radius $r_2 \approx 46$ km. Then, at $\rho_2 = 2.4 \times 10^{-2}$ kg/m^3, we have $P_c(r_1) = 1.5 \times 10^{14}$ W. The power flux of latent heat $\Pi_c = P_c/S_c$ where $S_c = \pi {r_1}^2$ is the surface area of condensation, close to 940 W/m^2. This value is comparable in magnitude to the solar constant (1370 W/m^2).

If the movement of the cyclone is taken into account, $P_c(r_1)$ increases by a factor of P_{T12}/P_{T11} times.

It should be noted that the powers of evaporation and condensation coincide.

5.4. TC Internal Energy

Following [72], the rate of change of internal energy in a TC elementary ring of area $2\pi rdr$ equates to the power spent on heating the air over the same surface area, which gives

$$c_p \rho H \frac{d\Delta t_2}{dt} = \lambda \rho_2 w \tag{21}$$

where $c_p \approx 10^3$ J/(kg·K) is the specific heat of air, Δt_2 is an increase in the air temperature in the TC (typhoon), $dt = \frac{dr}{\overline{u}} = \frac{dr}{k_2 u}$, $\overline{u}$ is the value of u averaged over altitude, $k_2 \approx 0.4$ is an empirical coefficient [72]. Rearranging Equation (21) and taking account of Equation (8) yields the following expression for the change in temperature:

$$\Delta t_2 = \Delta t_m \int \left(1 - \frac{u_0 \alpha}{u}\right) \frac{dr}{r} \tag{22}$$

where

$$\Delta t_m = \frac{\rho_2}{\rho} \frac{\lambda}{c_p k_2} \frac{h_0}{H}$$

After the integral in Equation (22) is performed, the following relation for the $r_0 \le r \le r_1$ ranges is obtained:

$$\Delta t_2(r) = \Delta t_2(r_0) - \Delta t_m \ln \frac{r}{r_0}(1 - \alpha_r) = \Delta t_m \ln \frac{\alpha r_1}{r(1 - \alpha_r)}. \tag{23}$$

Expression in Equation (23) shows that $\Delta t_2(r_1) = 0$ (since $w(r_1) = 0$) and $\Delta t_2(r_0) = \Delta t_m \ln(\alpha r_1 / r_0)$. At $h_0 = 500$ m, $H_0 = 7.5$ km we have $\Delta t_m \approx 10.8$ °C. At the center of a typical TC (typhoon), i.e., at $r = r_0$, $\Delta t_2(r_0) \approx 15$ °C. Observations show that the air temperature within a TC (typhoon) in reality exceeds the temperature of the air around it only by 3–4 °C. This occurs because a TC draws cold air in from the surrounding environment, and the latter has a mass exceeding the mass of air in a TC (typhoon) by a factor of a few times.

Assuming the mass of air in the cyclone core $m_1 = 2 \times 10^{15}$ kg and its average change in temperature $\overline{\Delta t_2}$ to be in excess of that predicted without accounting for the cold gas drawn in, we obtain the estimate for excess TC (typhoon) internal energy at $\overline{\Delta t_2} = 5$ °C as follows:

$$\Delta E_T = c_p m_1 \overline{\Delta t_2} \approx 10^{19} \text{ J}.$$

5.5. Power That TCs (Typhoons) Produce by Kinetic Frictional Forces between Air and the Oceanic Surface

The relations for the differential of the friction force and power are given by

$$dF_f = 2\pi C_D \rho V^2(0) r dr,$$
$$dP_f = 2\pi C_D \rho V^3(0) r dr$$

where $V(0)$ is the magnitude of the velocity at the oceanic surface, and $C_D \approx 1.7 \times 10^{-3}$ is the coefficient of kinetic friction between the wind and the oceanic surface [69]. Following [72], assume that $V(0) = v(0) \sec \chi$ where $v(0)$ is the value at the water surface. In addition, set $v(0) = k_3 v$ where $k_3 \approx 0.9$ is an empirical coefficient [72]. Then,

$$P_f = 2\pi C_D \rho k_3^3 \sec^3 \chi \int_{r_0}^{R} v^3(r) r dr$$

where (r) is given in (5). Performing the integral, we obtain

$$P_f = C_D \rho k_3^3 \sec^3 \chi v_0^3 S_{ef} \tag{24}$$

$S_{ef} = \frac{3}{2}\alpha^2 \pi R_0^2 \equiv k_4 \pi R_0^2$, $k_4 \approx 0.11$.
From Equation (24), $P_f \approx 2.5 \times 10^{13}$ W at v_0 = 60 m/s.

5.6. TC (Typhoon) Kinetic Energy Balance Equation

This meteorological object consumes heat from the ocean and increases its kinetic energy. Simultaneously, the cyclone transfers part of its energy to the oceanic surface layer due to air vortex friction. The balance equation is given by

$$\frac{dE_k}{dt} = \eta P_{T1} - P_f \tag{25}$$

where η is the energy loss rate or the part of the power that the heat source transfers to E_k, P_{T1}, and P_f, which are given in Equations (15) and (24). The balance equation and Equations (15) and (24) show that the power entering the TC is proportional to w_0, i.e., to v_0 and v_1, and the power lost from the TC is proportional to v_0^3. At steady conditions, ηP_{T1} = P_f, which takes place at the steady value of $v_0 = v_{s0}$. The value of the energy loss rate can be estimated from the following relation:

$$\eta = \frac{E_{k1} + E_{k2}}{\tau_s P_{T1}}$$

where τ_s is the TC development time. Calculations show that the values η ≈ 2.8–3.6%, depending on the cyclone intensity. A value of η = 3.6% is provided in [72].

It is convenient to rewrite the balance Equation (25) as

$$\frac{dv_0}{dt} = a_0 - b_0 v_0^2 \tag{26}$$

where $a_0 = c_1 \Delta T_1 \frac{\rho_1}{\rho} \frac{\eta h_1}{k_1 \alpha^2 \pi R_0 H} \left(\frac{h_0}{h} k_v + 2k_{11} \frac{v_1}{v_0} \right)$, $b_0 = \frac{3 C_D k_3^3 \sec^3 \chi}{2 k_1 H}$.

For the parameters of TCs presented above, estimates provide the magnitudes of the characteristic acceleration $a_0 \approx 5.2 \times 10^{-4}$ m·s^{-2} ≈ 45 m·s^{-1}·day^{-1} at v_1 = 0, which means that an increase in v_0 of about 45 m/s occurs over one day. If $v_1 \neq 0$, then an enhancement of the wind within the vortex occurs much more rapidly. The b_0 estimates are somewhat more complicated to perform because the coefficients C_D and k_3 remain approximately constant only for small v_0. In this case, $C_D \approx 1.7 \times 10^{-3}$, and $k_3 \approx 0.9$. Then, $b_0 \approx 3.2 \times 10^{-7}$ m^{-1} ≈ 2.7×10^{-2} m^{-1}·s·day^{-1}. At steady state, $a_0 = b_0 v_{s0}^2$, whence at v_1 = 0, we find that v_{s0} = 40 m/s. The coefficient C_D gradually increases with v_0, and its magnitude is doubled at v_0 = 30 m/s [68]. The dependence $k_3(v)$ is not known. With increasing v_0, the mechanical coupling between the wind and the oceanic surface layer apparently increases, but k_3 decreases, which is associated with a decrease in b_0, which would seem to increase the magnitude of v_{s0}. As will be shown below, the magnitude of v_{s0} is determined not at all by the processes accounted for in Equation (29) but by joint processes operating in the ocean–TC (typhoon) subsystem (see the relations in Equations (30) and (32)).

The energetics and thermodynamic parameters of a typical TC (typhoon) are presented in Tables 4 and 5.

Table 4. Energetics parameters of a typical typhoon.

Stored kinetic energy of the air rotational motion	$E_{k1} = \frac{m_{ef}}{2} v_0^2 = 2 \times 10^{18}$ J
Kinetic energy of translational motion at a speed of $v_1 = 7.5$ m/s	$E_{k2} = 0.4 \times 10^{18}$ J
Air internal energy increase (without accounting for advection and thermal advection)	$E_T = 10^{19}$ J
Power of water vapor condensation	$P_c = 1.5 \times 10^{14}$ W
Condensation power flux	$\Pi_c \approx 940$ W/m^2
Oceanic internal energy lost per unit time	$P_{T1} = 15.2 \times 10^{14}$ W
Oceanic internal energy lost over 6 days	$Q_1 = 7.9 \times 10^{20}$ J
Power for oceanic water evaporation	$P_{T2} \approx 11.4 \times 10^{14}$ W
Power for air heating	$P_{T3} \approx 3.8 \times 10^{14}$ W
Power that cyclone produces by frictional forces between air and the oceanic surface	$P_f \approx 2.5 \times 10^{13}$ W
Energy loss rate	$\eta \approx 3.5 \times 10^{-2}$

Table 5. Thermodynamic parameters in the ocean–atmosphere subsystem.

Water vapor density	$\rho_2 \approx 2.4 \times 10^{-2}$ kg/m^3
Air heating (without accounting for heat losses due to cold air advection and thermal advection)	$\Delta t_2 \approx 10$ °C
Real air heating	$\Delta t_2 \approx 3$–4 °C
Cooled water layer thickness	$h_1 = 80$ m
Surface area of cooled water	$2r_1 L \approx (0.5$–$2) \times 10^{12}$ m^2
Length of cooled water surface	$L = v_1 \tau_c \approx 3000$–$5000$ km
Duration of cooling (cyclone lifetime)	$\tau_c = 5$–7 days
Mean value of water temperature decrease in the oceanic surface layer	$\Delta t_1 = 2$–3 °C
Period of water temperature and air speed oscillations	$T = 15$ days
Characteristic time constant of the oscillation damping mentioned above	$\gamma^{-1} = 5$ days

6. Coupling of the Ocean and the Tropical Cyclone (Typhoon)

6.1. Governing Relations

Assume that the balance equation for the temperature of the oceanic water in the surface layer can be cast in the following form Ref. [9]:

$$\frac{dt_1}{dt} = -b_1(t_1 - t_{1m})v_0^2 + \frac{t_f - t_1}{\tau} \tag{27}$$

where $b_1 \approx 3 \times 10^{-4}$ m^{-2} s^2 day^{-1}, $\tau = 10$ days, t_f is the water temperature in the oceanic surface layer during the TC (typhoon) season (usually $t_f = 28$–30 °C), and t_{1m} is the temperature of cold-water layers (it may be assumed to be $t_{1m} = 23$ °C). The first term on the right-hand side of (27) describes the cooling of oceanic water due to its coupling to the meteorological object. The second term describes the relaxation of temperature in the layer mentioned above following the passage of the TC (typhoon).

Equation (27) must be solved along with a balance equation analogous to Equation (26). It should be noted that a TC develops only if $t_1 > t_c$, where $t_c \approx 26.5$ °C is a critical water temperature. We assume that the cyclone continues to consume oceanic heat also at $t_c > t_1 > t_{1m}$, consequently, Equation (26) is replaced by another equation given by

$$\frac{dv_0}{dt} = a_0 \frac{t_1 - t_{1m}}{t_f - t_{1m}} \left(1 + \frac{\kappa v_1}{v_0}\right) - b_0 v_0^2 \tag{28}$$

where $\kappa = 2\frac{h}{h_0}\frac{k_{11}}{k_v}$.

6.2. Steady-State Solutions

It is easy to show that the set of Equations (27) and (28) can describe nonlinear damped oscillations in the temperature, t_1, of the oceanic surface layer and in the tangential speed v_0 of the TC (typhoon) around the steady values of t_s and v_s. At other values of the parameters coupling the subsystems, the system may return to its equilibrium parameters t_s and v_s aperiodically. The latter are found from (27) and (28) at $d/dt = 0$, i.e., from the following set of equations:

$$-b_1(t_s - t_{1m})v_s^2 + \frac{t_f - t_s}{\tau} = 0 \tag{29}$$

$$a_0\frac{t_s - t_{1m}}{t_f - t_{1m}}\left(1 + \frac{\kappa v_1}{v_s}\right) - b_0 v_s^2 = 0 \tag{30}$$

In the following notations: $\theta_s = t_s - t_{1m}$, $\theta_f = t_f - t_{1m}$, $v_{c1}^2 = a_0/b_0$, $v_c^2 = (b_1\tau)^{-1}$, $B = \kappa v_1/v_s$, the set of Equations (29) and (30) may be rewritten as

$$\theta_s v_s^2 = v_c^2(\theta_f - \theta_s) \tag{31}$$

$$v_{c1}^2\frac{\theta_s}{\theta_f}\left(1 + \frac{\kappa v_1}{v_s}\right) = v_s^2 \tag{32}$$

Eliminating v_s from Equations (31) and (32), we obtain the relation for $y = \theta_f/\theta_s$ given by

$$1 + \frac{B_0}{\sqrt{y-1}} = A_0(y-1)y \tag{33}$$

where $A_0 = v_c^2/v_{c1}^2$, and $B_0 = \kappa v_1/v_c$. Let the solution to Equation (33) be y_0. Then,

$$v_s = v_c\sqrt{y_0 - 1}$$

In the case of an unmoving TC (typhoon), $v_1 = 0$, i.e., $B_0 = 0$, the solution to Equation (33) takes the form

$$\theta_s = \frac{1}{2}\theta_f A_0\left(\sqrt{1 + 4A_0^{-1}} - 1\right)$$

The formula for v_s is given by

$$v_s = \frac{v_c}{\sqrt{2}}\left(\sqrt{1 + 4A_0^{-1}} - 1\right)^{1/2}.$$

Generally, Equation (33) should be solved numerically. As an example, Table 6 illustrates the solutions for a typically developed TC (typhoon) obtained at $A_0 \approx 0.34$.

Table 6. In a steady-state case, the values of θ_s and v_s vs. the speed, v_1, of TC (typhoon) translational motion for a typically developed TC (typhoon).

Variables	**Values**								
v_1 (m/s)	1	3	5	10	15	20	25	30	35
θ_s (°C)	2.1	1.6	1.4	1.1	0.9	0.85	0.8	0.7	0.7
v_s (m/s)	28	34	36	43	46	49	51	53	55

6.3. Investigation of Steady-State Stability

Substituting $t_1 - t_{1m} = \theta_s(1 + \delta_\theta)$, $v_0 = v_s(1 + \delta_v)$, where $|\delta_\theta|$, $|\delta_v| << 1$, in Equations (27) and (28) yields the following linearized relations:

$$\frac{d\delta_v}{dt} = A_1(\delta_\theta - A_2\delta_v) \tag{34}$$

$$\frac{d\delta_\theta}{dt} = -B_1(\delta_v + B_2\delta_\theta) \tag{35}$$

where $A_1 = \frac{1}{\tau_s}\left(\frac{v_s}{v_{c1}}\right)^2$, $A_2 = \frac{2+3B}{1+B}$, $B_1 = \frac{2}{\tau}\frac{v_s^2}{v_c^2}$, $B_2 = \frac{1}{2}\left(1 + \frac{v_c^2}{v_s^2}\right)$, $\tau_s = v_s/a_0$ is a characteristic time constant for the development of a cyclone. Assuming the solutions to Equations (34) and (35) are proportional to $e^{\lambda t}$, we arrive at the quadratic characteristic equation whose solution is of the form given by

$$\lambda_{1,2} = -\gamma \pm \sqrt{\gamma^2 - \gamma_1^2}$$

where

$$\gamma = \frac{1}{2}(A_1A_2 + B_1B_2),$$

$$\gamma_1^2 = A_1A_2 + A_1A_2B_1B_2.$$

Taking into account the expressions for A_1, A_2, B_1, and B_2, we have:

$$\widetilde{\gamma} \equiv \gamma\tau = \frac{1}{2}\left(\frac{D}{2\mu}\frac{2+3B}{1+B} + \frac{1+B}{D}\right),$$

$$\widetilde{\gamma}_1^2 \equiv \gamma_1^2\tau^2 = \frac{2 + 2.5B - D}{\mu}$$

where $D = v_s^2/v_{c1}^2$, $\mu = \tau_s/2\tau$.

The relaxation of small disturbances in the oceanic water temperature and in the cyclonic air speed obeys an aperiodic law if $\widetilde{\gamma}^2 > \widetilde{\gamma}_1^2$, or the small disturbances relax as a damped nonlinear oscillator does if $\widetilde{\gamma}^2 < \widetilde{\gamma}_1^2$. The frequency of the oscillations is given by $\omega_1 = (\gamma_1^2 - \gamma^2)^{1/2}$. In the latter case, the condition $D < 2 + 2.5B$ must be satisfied at $\gamma_1^2 > 0$ as well. In addition, the inequalities $0 < D < 1$ must be always satisfied. In particular, we have $D < 2$ for a motionless cyclone ($B = 0$). For such a cyclone, the condition $\widetilde{\gamma}^2 < \widetilde{\gamma}_1^2$ yields $D < 1$. Consequently, damped oscillations arise when the $1 > D > 0$ inequalities are satisfied in the case of $v_1 = 0$. For example, the parameter μ is found within the limits from $(2 - \sqrt{3})/4 \approx 0.07$ to $(2 + \sqrt{3})/4 \approx 0.93$ at a value of $D = 0.5$.

7. General Information on the Role That Tropical Cyclones (Typhoons) Play in Couplings in the Ocean–Atmosphere–Ionosphere–Magnetosphere System

Cyclonic activity and oceanic surface waves are known to generate acoustic–gravity waves reaching 100–300 km in height and heating the domain of an upper atmosphere. The heating is accompanied, in particular, by changes in the conductivity σ_i of the ionospheric plasma at the ionospheric *E*-region dynamo heights (~100–150 km). The σ_i variations act to generate the geomagnetic disturbances that propagate to the magnetosphere, violate the adiabatic invariants of the energetic particles trapped in the radiation belts, and cause particle pitch-angle scattering and precipitation into the upper atmospheric layers. The ocean–cyclone–upper-atmosphere–ionosphere–magnetosphere–upper atmosphere coupling arises. Such a mechanism for coupling is naturally termed the acoustic–gravity one. Its reality, or rather the reality of individual links, is confirmed by the results of [10–13,18,19,23–27,71].

The second mechanism for subsystem coupling is based on electrodynamic processes. The cyclonic activity stimulates the intense evaporation of oceanic water, its subsequent condensation, the development of a powerful cloud structure, and the occurrence of thunderstorms [1,30,31,73–75]. A lightning stroke acts to heat electrons and to increase electron density in the lower ionosphere (50–100 km height). The electromagnetic radiation energy and power fluxes from lightning are large enough to restructure the upper atmosphere–ionosphere–magnetosphere subsystem coupling, to cause the precipitation of energetic particles from the Earth's radiation belts into the upper atmosphere and the subsequent secondary processes to occur [31]. The latter include, in particular, the following. The particle precipitation contributes to the plasma conductivity increase at the ionospheric *E*-region dynamo heights (~100–150 km), which causes changes in polarization electric fields, which penetrate the magnetosphere and interact with the energetic particles in the radiation belts, stimulating their precipitation further. This is how the repeated interaction between the subsystems is carried out by means of the electrodynamic mechanism.

The third mechanism is based on the appearance of the external current in thunderstorm clouds at 10–15 km heights with current densities exceeding the fair-weather current values by a few orders of magnitude. Consequently, the quasi-steady electric field increases by 1–2 orders of magnitude in the entire ionospheric column approximately over the TC and its neighborhood. Its presence was revealed and described in [5,6]. This electric field, slightly weakened, penetrates the magnetosphere and affects the motion of energetic charged particles in the geomagnetic trap. Under certain conditions, the electric field acts to precipitate some of these particles into the upper atmosphere. Further, a repeated coupling between the subsystems arises.

The full theory of coupling between the components of the Earth–atmosphere–ionosphere–magnetosphere has not been completed to date.

The mechanisms listed above (acoustic–gravity, electrodynamic, and electrical ones) are considered in detail below.

8. Acoustic–Gravity Wave Generation by the Ocean–Tropical Cyclone (Typhoon) Subsystem

8.1. AGW Amplitude and Spectrum

TCs (typhoons) generate turbulence. Due to the nonlinearity of hydrodynamic equations, turbulence serves as a source of AGWs in a broad frequency, Ω, range. The high-frequency ($\Omega > \omega_A$) and low-frequency ($\Omega < \omega_B$) components of AGWs are usually termed the acoustic and internal gravity waves (IGWs), respectively. Here, $\omega_A^2 = \gamma_a g/4H \equiv \alpha_0 \omega_B^2$, $\omega_B^2 = (\gamma_a - 1)g/\gamma_a H$, g is the gravitational acceleration, ω_A and ω_B are the cutoff frequencies for acoustic waves and IGWs, respectively. The frequency ω_B is also termed the Brunt–Väisälä frequency [76]. The formulae accounting for the atmosphere temperature variability in altitude can be cast in the following form:

$$\omega_A^2 = \frac{\gamma_a g}{4H}\left(1 + \frac{H}{T}\frac{dT}{dz}\right),$$

$$\omega_B^2 = \frac{g}{H}\left(\frac{\gamma_a - 1}{\gamma_a} + \frac{H}{T}\frac{dT}{dz}\right).$$

Here, T is the neutral atmospheric temperature.

It is advisable to evaluate the amplitude of air pressure pulsations, which are characterized by its root-mean-square value δp_m in order to study the effects that the TC (typhoon) has on the atmosphere and ionosphere. The partial differential equation for the pressure disturbance can be obtained from the continuity (density ρ), momentum (velocity v), and energy (pressure p) hydrodynamic equations retaining terms of order two (see, e.g., [76,77]). The problem of radiating AGWs has been solved for the first time by [78]; they have shown that the radiation of AGWs is generated mainly by two-dimensional isotropic turbulence

and that the quadrupole radiation predominates the dipole component. Following [78], one can obtain a relation for the r.m.s. value of the pressure disturbance, given by

$$\delta p_m(R) = \frac{C_0^{1/2} k_V}{8\sqrt{2}\pi} \frac{\rho_0 h \varepsilon^{19/12}}{\nu_0^{3/4}} \frac{R_0}{R} \left(\frac{V_0}{l}\right)^{1/3} I^{1/2}, \; \varepsilon = \frac{\widetilde{v}^3}{l} \tag{36}$$

where $C_0 \approx 2$ is a universal constant, h is a TC (typhoon) thickness, R is the distance from the typhoon center, ρ_0 is the undisturbed air density at the surface of the water, $\nu_0 \approx 1.4 \times 10^{-5}$ m^2/s is the kinematic viscosity coefficient for air, $\omega_B \approx 1.7 \times 10^{-2}$ s^{-1}, $\widetilde{v}$ are fluctuations in the flux velocity, V_0, due to turbulence ($\widetilde{v}$ is usually an order of magnitude smaller than V_0), $k_V = r_r/R_0$, r_r is the radius of the TC (typhoon) core effectively radiating AGWs, $l \approx R_0$ is the external turbulence scale, ε is a turbulence power density, and I is the integral given by

$$I = \int_{x_1}^{x_2} \left(\frac{\alpha_0 - x^2}{1 - x^2}\right)^{2/3} \frac{dx}{(1 - x^2)x^{7/3}}. \tag{37}$$

Here, $x_1 = \Omega_1/\omega_B$, $x_2 = \Omega_2/\omega_B$, Ω_1 and Ω_2 are the minimum and maximum frequencies in the IGWs spectrum. The relation in (37) shows that the radiation intensity exhibits sharp increases in the $x \to 0$ and $x \to 1$ limits, i.e., at the vicinity of the frequencies Ω_1 and $\Omega_2 \approx \omega_B$, respectively, which pertain to the IGW range of frequencies. The frequency Ω_1 is determined from the condition $\Omega_1 t_0 >> 1$, where $t_0 = l/V_0$ is a characteristic time [78], and $\Omega_1 \approx 10\, V_0/l$, $x_1 \approx (3\text{–}6) \times 10^{-2}$. It is important that $\Omega_1/\Omega_2 \approx (1.7\text{–}3.4) \times 10^{-2} << 1$.

Although the radiation efficiency of the quadrupole sharply increases at $\Omega \to \omega_B$, the attenuation of IGWs simultaneously increases as well. Therefore, only the emission of waves in the vicinity of the frequency Ω_1 is of practical interest. For $\Omega \approx \Omega_1$, we have

$$I^{1/2} = \frac{\sqrt{3}}{2} \frac{\alpha_0^{1/3}}{c_{s0}^{2/3} \omega_B} \left(\frac{l}{k_\omega V_0}\right)^{2/3} \tag{38}$$

where $c_{s0} \approx 340$ m/s is the speed of acoustic waves in the air. Substituting Equation (38) into Equation (36) yields:

$$\delta p_m = A_p \frac{R_0}{R} \frac{\widetilde{v}^{19/4} V_0^{-1/3}}{l^{5/4}}, \; A_p = \frac{\sqrt{3} C_0^{1/2} \alpha_0^{1/3} k_V}{16\sqrt{2}\pi k_\omega^{2/3}} \frac{\rho_0 h}{\nu_0^{3/4} c_{s0}^{2/3} \omega_B}, \; \widetilde{v} \approx 0.1 V_0 \tag{39}$$

where $k_\omega = \Omega_1\, l/V_0 \approx 10$ is a dimensionless coefficient.

It is important that Δp_m is proportional to $\widetilde{v}^{53/12}/Rl^{1/4}$. Since $\widetilde{v}^{53/12}$ decreases very rapidly with distance from the internal boundary of a TC, the radius of the cyclone core effectively radiating IGWs is estimated to be $r_{ef} \approx 2\, r_0$ and $k_V \approx 1/20$. At the vicinity of the source (i.e., at $R \approx R_0$, $l \approx R_0$), the estimate of Δp_m can be obtained from Equation (39), as given by

$$\delta p_m(R_0) \approx \frac{V_0^{53/12}}{{R_0}^{5/4}}$$

where V_0 is in m/s, R_0 is in m, and δp_m is in Pa. The calculation of the power of IGW radiation based on $\delta p_m(R_0)$ involves the integration of the energy flux Π_r over the half-sphere of radius R_0. Taking into account the antenna pattern of the radiator, this surface area is of the order of $S_0 = \pi R_0^2$. Table 7 gives the results of calculations on the basic parameters of the coupling subsystems vs. the energy of the primary source, the oceanic surface layer.

Table 7. Dependence of the main parameters of the ocean–tropical cyclone (typhoon) subsystem vs. the internal energy lost by the ocean (the magnitude of the wind within the cyclone).

v_0 (m/s)	15	20	25	30	35	40	50	60	70	80	90
u_0 (m/s)	4.8	6.4	8	9.6	11.2	12.8	16	19.2	22.4	25.6	28.8
V_0 (m/s)	15.8	21	26.3	31.5	36.8	42	52.5	63	73.5	84	94.5
w_0 (cm/s)	1.8	4.8	10.8	19.2	28	36	42	47	52	53	53
v_1(m/s)	3	4	5	6	7	8	10	12	14	16	18
h_0 (m)	50	100	200	300	400	500	500	500	500	600	700
r_0 (km)	10	10	11	11	12	13	14	15	16	18	20
r_1 (km)	147	157	167	176	185	196	211	226	241	259	278
R_0 (km)	400	425	450	475	500	530	570	610	650	700	750
r_2 (km)	30	32.5	34	36.5	38	40	43	46	49	52	55
$S_0 \times 10^{-11}$ (m^2)	5	5.7	6.4	7.1	7.9	8.8	10.2	11.7	13.3	15.4	17.7
$m_{ef} \times 10^{-14}$ (kg)	3	3.4	3.8	4.3	4.7	5.3	6.1	7	8	9.2	10.1
$m \times 10^{-15}$ (kg)	5	5.7	6.4	7.1	7.9	8.8	10.2	11.7	13.3	15.4	17.7
$E_{k1} \times 10^{-18}$ (J)	3.4×10^{-2}	6.8×10^{-2}	1.1×10^{-1}	1.9×10^{-1}	2.9×10^{-1}	4.2×10^{-1}	7.6×10^{-1}	1.3	2	2.9	4.1
$E_{k2} \times 10^{-18}$ (J)	2.2×10^{-2}	4.6×10^{-2}	8×10^{-2}	1.3×10^{-1}	1.9×10^{-1}	2.8×10^{-1}	5×10^{-1}	8.4×10^{-1}	1.3	2	2.9
$E_k \times 10^{-18}$ (J)	5.6×10^{-2}	1.1×10^{-1}	1.9×10^{-1}	3.2×10^{-1}	4.8×10^{-1}	7×10^{-1}	1.3	2.1	3.3	4.9	7
$\overline{\Delta T_1}$ (K)	1	1.3	1.5	2	2.1	2.4	2.4	2.4	2.5	2.5	2.5
h_1 (m)	20	30	50	60	70	80	80	80	80	80	85
$P_{T11} \times 10^{-14}$ (W)	3.3×10^{-2}	9.3×10^{-2}	2.4×10^{-1}	4.8×10^{-1}	7.3×10^{-1}	1.1	1.6	2	2.5	3.1	3.6
$P_{T12} \times 10^{-14}$ (W)	2.3×10^{-1}	0.7	1.6	3.2	4.9	7.3	8.5	13.2	16.7	20.4	26.5
$P_{T1} \times 10^{-14}$ (W)	2.6×10^{-1}	0.8	1.8	3.7	5.6	8.4	9.6	15.2	19.2	23.4	30.1
$P_f \times 10^{-14}$ (W)	1.7×10^{-3}	4.6×10^{-3}	10^{-2}	1.9×10^{-2}	3.4×10^{-2}	5.6×10^{-2}	1.3×10^{-1}	2.5×10^{-1}	4.6×10^{-1}	7.9×10^{-1}	1.3
η (%)	3.4	3.6	3.4	3.4	3.4	2.4	3	2.8	2.8	3	3.2
τ_s (day)	6.6	4.2	4	3.4	2.8	2.4	2	1.6	1.4	1.1	1
$\Delta p(r_0)$ (hPa)	6	9.7	14.2	19.7	26	33.2	50	84.8	93.1	148	184
$P_c \times 10^{-14}$ (W)	2.5×10^{-2}	7.2×10^{-2}	1.8×10^{-1}	3.6×10^{-1}	5.6×10^{-1}	8.5×10^{-1}	1.1	1.5	1.9	2.3	2.7
Δt_2 (°C)	12.1	12.6	12.2	12.7	12.5	12.2	12.2	12.2	12.2	11.8	11.6
$P_{T2} \times 10^{-14}$ (W)	3.3×10^{-2}	9.6×10^{-2}	2.4×10^{-1}	0.5	7.5×10^{-1}	1.1	1.6	2	2.5	3.7	5
$\delta p_m(R_0)$ (Pa)	1.6×10^{-2}	5.1×10^{-2}	1.3×10^{-1}	2.7×10^{-1}	0.5	0.84	2.1	4.3	7.7	12.9	19.6
$v_w(R_0)$ (mm/s)	3.6×10^{-2}	1.2×10^{-1}	2.9×10^{-1}	6.1×10^{-1}	1.1	1.9	4.7	9.7	17.4	29.2	44.3
Π_r (W/m^2)	5.7×10^{-7}	5.9×10^{-6}	3.8×10^{-5}	1.6×10^{-4}	5.7×10^{-4}	1.6×10^{-3}	9.5×10^{-3}	4×10^{-2}	1.3×10^{-1}	3.8×10^{-1}	0.9
$P_r \times 10^{-12}$ (W)	2.9×10^{-7}	3.4×10^{-6}	2.4×10^{-5}	1.1×10^{-4}	4.5×10^{-4}	1.4×10^{-3}	9.5×10^{-3}	4.5×10^{-2}	1.7×10^{-1}	5.8×10^{-1}	1.6
$S_r \times 10^{-12}$ (m^2)	0.5	0.57	0.64	0.71	0.79	0.88	1	1.12	1.33	1.54	1.77
z_0 (km)	280	250	230	220	200	195	180	160	140	120	105

Table 7 presents the δp_m, Π_r, and P_r estimates. It can be seen that the pressure variations in IGWs from a TC begin to exceed the atmospheric pressure noise level (of about 0.5–0.7 Pa [78]) at $v_0 \geq 35$–40 m/s, i.e., when a tropical storm evolves into a hurricane (typhoon).

8.2. IGW Prevalent Periods

The fundamental frequency ω_B of IGW mode corresponds to a period of about 6 min. As mentioned above, waves with such periods are highly attenuated. Therefore, the waves at frequencies of the order of Ω_1 should be propagated at large distances from cyclones. The frequency Ω_1 corresponds to the period $T_{r1} \approx 2\pi l/10\, V_0 \approx 0.6\, l/V_0 \approx 0.6\, R_0/V_0$. For instance, at $\widetilde{v} = 6$ m/s and $l = 500$ km, we have $T_{r1} \approx 5.2 \times 10^3$ s ≈ 1.45 h. This period is very close to the period of, on average, 1.5 h observed by [79].

8.3. Infrasound Generation by Oceanic Waves

There is another channel for the effective impact of the ocean–TC (typhoon) subsystem on the upper atmosphere. The fact is that the movement of this meteorological object is accompanied by intense oceanic waves. The wave height attains 13–14 m [72]. The waves, in turn, are a source of noise-like acoustic radiation. The radiation intensity maximum occurs at the frequency f_m, which is related to the wind speed in the cyclone by the relation [80]:

$$f_m = \frac{2\sqrt{2}}{6\pi}\frac{g}{V}.$$

This frequency corresponds to the period $T_{max} = f_m^{-1}$. The acoustic radiation energy flux has been calculated in [80]:

$$\Pi_a = \frac{27\pi}{32}\frac{\rho M^2 g^2}{c_{s0}^3}\left(\frac{V}{2g}\right)^8 \cos\theta$$

where θ is the angle between the wave vector and the normal to the oceanic surface, $M = 3.05$ m^2/s^5.

The results of calculations on such parameters of acoustic radiation as $\Pi_{a0} = \Pi_a(\theta = 0)$, the pressure oscillation amplitude $\delta p_a = (\rho_0 v_{s0}\Pi_{a0})^{1/2}$, the speed amplitude of particulates

in the wave $v_w = \delta p_a / \rho_a c_{s0}$, f_m, $T_{\max}$, and the infrasonic radiation power P_a are presented in Table 8. Since $\Pi_{a0} \sim V^8$, the cyclone core, where V is close to $V_0(r_0)$, gives the main contribution to the radiated power. The core radius is assumed to be $r_a = 1.5\, r_0$, and the radius r_a corresponds to the surface area of $S_a = \pi r_a^2$.

Table 8. Main parameters of acoustic radiation generated by oceanic waves.

V_0 (m/s)	f_m (mHz)	$T_{\max}$ (s)	Π_{a0} (W/m^2)	δp_a (Pa)	v_w(m/s)	$S \times 10^{-9}$ (m^2)	P_a (W)
10	147	6.8	3.7×10^{-7}	1.3×10^{-2}	2.9×10^{-5}	0.7	2.6×10^{2}
15	98	10.2	9.2×10^{-6}	6.4×10^{-2}	1.4×10^{-4}	0.7	6.5×10^{3}
20	74	13.6	9.2×10^{-5}	0.2	4.5×10^{-4}	0.7	6.5×10^{4}
25	59	17	5.5×10^{-4}	0.5	1.1×10^{-3}	0.85	4.7×10^{5}
30	49	20.4	2.4×10^{-3}	1	2.3×10^{-3}	0.85	2×10^{6}
35	42	23.8	8.1×10^{-3}	1.9	4.3×10^{-3}	1	8.1×10^{6}
40	37	27.2	2.4×10^{-2}	3.3	7.5×10^{-3}	1.2	2.9×10^{7}
50	29	34	0.14	7.9	1.8×10^{-2}	1.4	2×10^{8}
60	25	40.8	0.6	16.3	3.7×10^{-2}	1.6	9.6×10^{8}
70	21	47.6	2.1	30.4	6.9×10^{-2}	1.8	3.8×10^{9}
80	18	54.4	6	51.4	0.12	2.3	1.4×10^{10}
90	16	61.2	15.5	82.7	0.19	2.8	4.3×10^{10}

9. Tropical Cyclone (Typhoon) Effect on the Upper Atmosphere

9.1. Upper Atmospheric Heating by IGWs

It has been demonstrated above that a TC (typhoon) is a source of intense IGWs. The latter, propagating upward, interact with the upper atmospheric layers, heating them. The effective heat transport from IGWs to the neutral atmosphere begins at the reference altitude z_0 where the particle speed in the wave begins to exceed a value of about $0.1 c_{s0}$ and the wave becomes nonlinear [14,81]. The greater the IGW intensity, the smaller the altitude z_0 (see Table 7). It is important that

$$v_w(z) = v_w(0) \exp(\zeta),\ \zeta = \frac{1}{2} \int_0^z \frac{dz}{H(z)}.$$

The $v_w(0)$ estimates, i.e., the value of v_w at the water surface, are presented in Table 8.

The heating of the upper atmospheric gas over a TC (typhoon) can be determined from the following balance equation:

$$\frac{dT}{dt} = \frac{\Pi}{c_p \rho H} - \frac{T - T_0}{\tau_T} \tag{40}$$

where τ_T is the relaxation time for the atmospheric temperature, T and T_0 are disturbed and undisturbed atmospheric temperatures, and Π is the AGW energy flux, which is given by

$$\Pi = \frac{\delta p^2}{\rho c_s}$$

where δp is the variation in air pressure due to AGWs. Given the meteorological object size scale of 2 $R_0 \approx$ 800–1200 km, the divergence of AGW rays is insignificant up to the heights of $z \sim 100$ km, and therefore $\Pi(z) \approx \Pi(0) = \delta p^2(0)/\rho(0) c_s(0)$ can be accurately assumed to be applicable up to the beginning of the region dissipating the AGW energy. Assuming the perturbation δp is caused by a monochromatic wave and the nonlinear distortions of

the wave profile are insignificant (this is true for $z \leq z_0$, i.e., $\delta p(z)/p_0(z) << 1$ where $p_0(z)$ is undisturbed air pressure), the variations in δp are modeled as

$$\delta p = \delta p_m \cos \Omega t \tag{41}$$

where δp_m and Ω are the amplitude and frequency of AGWs, respectively. Thus

$$\Pi(t) = \Pi_m \cos^2 \Omega t = \frac{\Pi_m}{2}(1 + \cos 2\Omega t). \tag{42}$$

Here,

$$\Pi_m = \frac{\delta p_m^2(0)}{\rho(0) c_s(0)} \tag{43}$$

is the AGW energy flux at the oceanic surface. Taking account of the relation in Equation (42), the solution to Equation (40) subject to the initial condition $T(t = 0) = T_0$ can be cast in the following form

$$\vartheta = \vartheta_m \left[1 - e^{-t/\tau_T} + \frac{\vartheta_m}{\Omega_T} \cos(2\Omega t - \varphi_\Omega) \right] \tag{44}$$

where $\vartheta = T/T_0 - 1$ is a relative perturbation of T, $\Omega_T = \Omega \tau_T$, $\mathrm{tg}\varphi_\Omega = 2\Omega_1$, and

$$\vartheta_m = \frac{T_m}{T_0} - 1 = \frac{\Pi_m \tau_T}{2 c_p \rho H T_0} \tag{45}$$

is the amplitude of ϑ.

It is to be noted that Equation (40) does not allow for thermal conductivity, whereas Equation (40) becomes nonlinear at $\vartheta \sim 1$. The thermal conductivity is negligible if its characteristic time $\tau_{TC} = H^2/\kappa_T >> \tau_T$, where κ_T is the coefficient of thermal conductivity. This inequality is satisfied at $z \leq 200$ km altitudes; here, $H \approx 40$ km, $\kappa_T \approx 5 \times 10^4$ m^2 s^{-1}, and $\tau_{TC} \approx 3 \times 10^4$ s. The magnitude of τ_T is dependent on the wind speed w_w in the upper atmosphere. If $w_w = 100$ m/s, the TC size $2\,R_0 \approx 1000$ km, $\tau_T = 2\,R_0/w_w \approx 10^4$ s. It is seen that $\tau_{TC} > \tau_T$.

The estimations of Π_m can be made using the formula in (43). At $\delta p_m \approx 20$ Pa [79], we have $\Pi_m \approx 0.9$ W/m^2. Then, the relation in (45) shows that the linear approximation is still applicable at 90 km altitude where $T_0 = 200$ K, $\rho \approx 4 \times 10^{-6}$ kg/m^3, $H \approx 8$ km, $\Delta T_m = T_m - T_0 \approx 140$ K, i.e., $\vartheta_m \approx 0.7$. In fact, the ΔT magnitude has been somewhat overestimated since the reflection, refraction, and other effects were not accounted for in the propagation of IGWs from the TC (typhoon) to the upper atmosphere. In any case, a few tens of percent increase in temperature should be expected over the meteorological object. Almost the same thermal effect is expected at the altitudes $z \geq z_0$ (up to $z \approx 200$ km where the thermal conductivity leads to a considerable decrease in ΔT).

Consider Equation (44). It is seen that the temporal variations are both periodic and aperiodic. The former are due to a turn-on transient, and the latter are due to a harmonic disturbance. At $t >> \tau_T$, we have

$$\vartheta \approx \vartheta_m \left(1 + \frac{\vartheta_m}{\Omega_T} \cos(2\Omega t - \varphi_\Omega) \right). \tag{46}$$

It is important that the frequency of variations in $T(t)$ is 2 times greater than the frequency of variations in $\delta p(t)$. In addition, the former exhibit the phase delay relative to the latter. Consider the φ_Ω magnitude. For the periods, T_w = 1.5–2 h, of IGWs, the frequency $\Omega \approx 10^{-3}$ s^{-1}. Then, $2\Omega\tau_T \approx 20 >> 1$. This means that $\varphi_\Omega \approx \pi/2$, i.e., the $T(t)$ disturbance is delayed by a quarter IGW period relative to the changes in $\delta p(t)$. At the T_w magnitudes specified above, the time delay is $T_w/4 \approx$ 25–30 min.

It is noted that the modulation amplitude $\vartheta(t)$ is significant if ϑ_m/Ω_T is close to 1, i.e., at both $\vartheta_m \sim 1$ and $\Omega_T \sim 1$. The latter takes place at the same magnitude of the IGW period

and $\tau_T \approx 10^3$ s, i.e., at the meteorological process characteristic scale of the order of 100 km. In this case, the time delay decreases to 20–25 min.

This kind of reasoning cannot describe the process of wave-medium nonlinear interactions comprehensively and strictly. The modern theory of such coupling is presented in [82].

9.2. Heating the Upper Atmosphere by Acoustic Waves

The infrasound generated by both oceanic waves and cyclone turbulence dissipates its energy on reaching the upper atmosphere and consequently heats the atmosphere at a wide range of altitudes. The dissipation of infrasound begins at the altitude z_{a1} where $v_w \approx 0.1\ c_{s0}$ and ceases at the altitude z_{a2} where the gas molecule collisional mean free path l_n is given by $l_n \approx \lambda_m = c_{s0}\ T_{\max}$ [14]. The acoustic radiation with the wavelength of $\lambda_m \approx$ 2–30 km reaches $z_{a2} \approx$ 330–430 km altitude, respectively. The magnitude of z_{a1} essentially depends on the magnitude of V_0, viz., for $V_0(r_0) \approx$ 20–90 m/s, the altitude $z_{a1} \approx$ 300–60 km, respectively.

The magnitude of ϑ_m can be estimated from the following relation analogous to that in Equation (45):

$$\vartheta_m = \frac{\Pi_a e^{-\Gamma} \tau_T}{2 c_p \rho H T_0} \times \frac{S_a}{S_0}$$

where the absorption of infrasound (Γ is the integral rate of absorption of energy in the wave) and the finiteness of the oceanic surface area that generates infrasound are accounted for. If $S_a << S_0$, the efficiency of heating in the core is low. Large pressure, δp_a, and particle speed, v_w, changes in the wave take place here. However, at $v_w \geq 0.1\ c_{s0}$, the wave profile begins to noticeably differ from the cosine law relation, and the frequency spectrum becomes enriched with high frequencies. The infrasound at the higher frequencies is absorbed at the lower altitudes where the gas number and mass densities are higher. This leads to a significant weakening of the wave, but insignificant gas heating. Therefore, the stronger perturbation in the upper atmosphere takes place not over the core of a strong cyclone (hurricane or typhoon) but closer to its periphery where V is less than V_0 by a factor of a few times. Despite the magnitude of Π_a is less here, the magnitude of Γ, which is in the exponent, is significantly smaller. In addition, in this case, the value of S_a is comparable in magnitude with S_0. All these factors lead to an increase in ϑ_m over some middle part of the TC where $r \approx$ (10–15) r_0.

The neutral gas heating by acoustic radiation causes a myriad of the already mentioned secondary processes, analogous to those caused by IGW dissipation in the upper atmosphere.

9.3. Geomagnetic Effect of IGWs

The upward propagating IGWs have a dual effect on the atmosphere. The linear wave propagation takes place at $z < z_0$ where IGWs only modulates the parameters of the neutral gas and plasma. At $z > z_0$, nonlinear IGW dissipation, which is added to the modulation, leads to heating the medium. Moreover, the medium temperature turns out to be modulated with the doubled frequency in the first approximation. The additional heating and temperature modulations cause, in turn, the changes and modulation of temperature-dependent plasma parameters, viz., collision frequencies, chemical reaction rates, electron and ion densities, etc. As a result, both the plasma conductivity tensor and dynamo current density become disturbed and modulated. A 10–100% change in the gas temperature also results in tens of percent perturbations in both the ionospheric conductivity tensor components and integral ionospheric currents. When a turn-on transient has ceased, the amplitude of the oscillations of the geomagnetic induction at the frequency 2Ω can be estimated using the following relation:

$$\Delta B_\Omega \approx \frac{\vartheta_m}{2\Omega_T}\mu_0 I_0, \tag{47}$$

where $\mu_0 = 4\pi \times 10^{-7}$ H/m is the magnetic permeability of a vacuum, I_0 is the undisturbed integral current. Assuming $I_0 = 0.02$ A/m, $\Omega = 10^{-3}$ s^{-1}, $\tau_T = 10^4$ s for the daytime conditions at low latitudes where typhoons pertain to, we obtain $\Delta B_\Omega \approx 0.13$–$1.3$ nT for $\vartheta_m = 0.1$–1, respectively. A close magnitude of ΔB_Ω was observed, for instance, in [79] where the calculations of the geomagnetic effect of IGWs are made in the linear approximation in detail.

At night, the current I_0 is an order of magnitude smaller, which means that the variations in ΔB_Ω are also an order of magnitude smaller. It is important to note that the relation in (47) is applicable to describing the magnetic effect of the infinite plane current sheet. The effect of the ground is also not accounted for.

The mechanism involving the IGW field drag on the charged particles [83] is a more efficient mechanism than that due to the modulation of ionospheric currents by IGW. The modulation of the ionospheric currents model provides the amplitude of the magnetic effect of the order of 1–10 nT.

9.4. Geomagnetic Effect of Acoustic Waves

The physical mechanism of the effect that infrasound has on the upper atmosphere is analogous to the mechanism for the IGW action. The upper atmospheric response to these impacts is also similar. The difference lies in the magnitudes of the prevailing periods of variations in the geomagnetic induction. The impact of infrasound should lead to enhancements in a geomagnetic pulsation level in the period range from unities to tens of seconds (see Table 8). The effect is noticeably pronounced only at the infrasound fundamental frequency ($\Omega \approx 0.1$–1 s^{-1}) at which $\Delta B_\Omega \sim 0.1$–1 nT (in the daytime). The magnitude of ΔB_Ω at the doubled frequency is 2–3 orders of magnitude smaller than at Ω (see Equation (47)).

10. Generation of Electromagnetic Radiation by Tropical Cyclones (Typhoons): Impact on the Magnetosphere and Radiation Belts

The development of TCs (typhoons) is accompanied by strong thunderstorms, and hence by the generation of electromagnetic radiation in a wide frequency band ($f \leq 100$ kHz). This is evidenced, in particular, by rocket and satellite observations (see, e.g., [28,80,84]). The energy and power of the strongest lightning stroke is of the order of 10 GJ and 10 GW. During a TC (typhoon) lifetime, the number of lightning strokes can attain 10^3–10^4, and their total energy and power can approach 10^2 TJ and 10^2 TW. About 10^{-3} the lightning stroke energy is transformed into acoustic wave energy, and approximately 10^{-4}–10^{-3} the lightning stroke energy is transformed into the electromagnetic wave energy. The total energy of these waves generated by 10^4 lightning strokes is 100 GJ and 10–100 GJ, respectively. The power of these radiations averaged over the cyclone lifetime (6 days) approaches 200 kW and 20–200 kW, respectively. The acoustic and electromagnetic energy fluxes reach the upper atmosphere (~50–100 km) and significantly change its parameters. In addition, the lightning-induced VLF radiation is transmitted along the geomagnetic flux tubes into the magnetosphere where energetic particles (electrons and protons) are trapped. As a result, the cyclotron instabilities are produced, the cyclotron waves and the energetic particles interact, and the energetic particles precipitate from the geomagnetic trap into the upper atmosphere [1,15,30,31,73–75]. The equations governing the variations in Alfvén wave or VLF emission energy fluxes w_e and in the number of energetic particles in the geomagnetic flux tube containing the wave source are given by [15]:

$$\frac{dw_e}{dt} = I_w + \Gamma_w n w_e - \gamma_w w_e, \tag{48}$$

$$\frac{dn}{dt} = I_n - \gamma_n n w_e \tag{49}$$

where I_w is the power of a radiation source, I_n is the source of energetic particles, ν_w^{-1} is the relaxation time of a wave energy flux w_e; Γ_w, γ_n are the coupling coefficients. It is important to note that the set of Equations (48) and (49) is nonlinear. The solutions to this set of equations are presented in [2,85], which show that the precipitation effect can be significant. Moreover, this effect pertains to the trigger ones. The coefficient of triggering has been estimated to be of the order of 10^2–10^3.

The VLF- or Alfven-wave-induced electron or proton precipitation, respectively, acts to produce additional ionization in the upper atmosphere to modulate the electrojet current, which, in turn, is a source of low-frequency emissions. Further, the secondary processes mentioned above develop in the subsystems. In this way, the impact of cyclones on the magnetosphere and the radiation belts proceeds, and the latter have an inverse impact on the underlying regions of the near-Earth environment.

11. Generation of Quasi-Steady Electric Fields: Impact on the Magnetosphere and Radiation Belts

11.1. Oceanic Aerosols

Aerosols are solid or liquid particulates 0.05 μm to 50 μm in diameter, d_a, [86,87]. Aerosols are formed via a range of mechanisms. The largest aerosols ($d_a > 1$ μm) are produced either by $V > 7$ m/s speed winds separating aerosols from the wave crests, or they are generated by a collapse of the bubble cavity and ejected (from the sea surface) in the form of a vertical jet (jet droplets). Under quiet conditions, the aerosol number, n_a, and mass, ρ_a, densities do not exceed 5×10^4 m^{-3} and 5×10^{-11} kg/m^3. The smaller ($d_a < 1$ μm) aerosols are formed mainly at the moment of bursting of the films of air bubbles ascending to the surface. Another way of forming aerosols with the sizes mentioned above is the rupture of large bubbles, generating numerous small bubbles (<100 μm), although they are frequently carried down the surface. The aerosol size distribution function attains a maximum value at $d_a \approx 0.1$ μm. Under quiet conditions, $n_a \approx$ (3–5) $\times 10^8$ m^{-3}, and $\rho_a \approx$ (3–5) $\times 10^{-10}$ kg/m^3 [86]. That is why the aerosol with $d_a \approx 0.1$ μm play the main role in the effects discussed below.

Strong winds in a TC (typhoon) contribute to more intense aerosol production. The following empirical relation is true for the total mass density of aerosol of all scale sizes [86]:

$$\ln\rho_a = 0.16V + 1.45 \tag{50}$$

or

$$\rho_a(V) = \rho_{a0} e^{\alpha_a V}$$

where $\rho_{a0} = 4.3 \times 10^{-9}$ kg/m^3, $\alpha_a = 0.16$ m^{-1}·s. The range of applicability of the formulae in (50) is not known; however, ρ_a increases by about two and a half orders of magnitude and attains $\rho_a \approx 10^{-6}$ kg/m^3, while $n_a \approx 10^{11}$ m^{-3}, already at $V = 35$ m/s (transition to hurricane, typhoon).

11.2. Electric Current in the Atmosphere

The average electric current density through the fair-weather atmosphere has a value of $j_0 \approx 3 \times 10^{-12}$ A/m^2 [86,88]. The continuity equations for positive and negative ions are analogous and may be written in the following form:

$$\frac{dn_i}{dt} = q_i - \alpha_i n_i^2 - \beta_a n_a n_i$$

where q_i is the ion production rate, $\alpha_i = 1.6 \times 10^{-12}$ m^3/s is the reaction rate constant, $\beta_a = 1.65 \times 10^{-2}$ m^3/s is the rate of ion attachment to aerosols. In the absence of the latter at a steady state, $n_{i\infty} = (q_i/\alpha_i)^{1/2}$. Under quiet conditions, $q_{i0} \approx 10^7$ m^{-3} s^{-1}, and

we have $n_{i\infty} \approx 2.5 \times 10^9$ m^{-3}. When $n_a \neq 0$, virtually all ions attach to aerosols over a time interval of $\tau_a = (\beta_a n_a)^{-1} \sim 10^{-7}$ s, resulting in the charge density $Q_0 = en_{i\infty}$ equal to about 4×10^{-10} C/m^3. At the convection speed w, the separated charges would generate the electric current $j_{a0} = Q_0\, w = en_{i\infty}w$. At $n_{i\infty} = 2.5 \times 10^9$ m^{-3} and $w = 0.6$ m/s, we have $j_{a0} = 2.4 \times 10^{-10}$ A/m^2. However, a significant charge separation does not occur under quiet conditions and $j_{a0} \approx j_0 \approx 3 \times 10^{-12}$ A/m^2.

Within a developed TC (typhoon), the situation can change dramatically when the production of aerosols, their electrification, charge separation, etc., activate significantly.

The mechanisms for aerosol electrification are listed in [87]. For TCs (typhoons), droplet spraying seems to be the main mechanism. The ascending air currents in a cyclone transport positively charged aerosols upward. The larger negatively charged droplets move downward. As a result, the current density increases significantly. An increase in precipitation results in a considerable enhancement in j_a. During heavy rains usually accompanying TCs (typhoons), the value of j_a attains 10^{-8} A/m^2 or even 10^{-7} A/m^2 [1,86].

The predominance of the concentration of ions of one sign over the other ensures the emergence of an uncompensated space charge (usually positive). Its magnitude can significantly exceed the background value of ~10^{-10} C/m^3. At the cyclone core, the current density approaches $j_a \approx 10^{-7}$ A/m^2 in a thunderstorm occurring in a cumulonimbus cloud. At the same magnitude of w, this value of the electric current corresponds to $Q = j_a/w \approx 1.7 \times 10^{-7}$ C/m^3 and to the rate of charge separation of $\dot{Q} = j_a/H_a \approx 10^{-11}$ A/m^3 where the dot over Q designates a time derivative. Here, H_a is the cloud thickness, usually $H_a \approx 10$ km. These values should be the upper bounds. The more probable values are $j_a \approx 3 \times 10^{-9}$–$3 \times 10^{-8}$ A/m^2 and $\dot{Q} \approx 3 \times 10^{-13}$–$3 \times 10^{-12}$ A/m^3. It is important to note that $j_a/j_0 \approx 10^3$–10^4 even in this case. The emerging powerful electric current generates a quasi-stationary electric field in the upper atmosphere, ionosphere, and magnetosphere [5,6].

11.3. Generation of Electric Fields

The processes acting in the atmosphere with characteristic times greater than $t_0 = \varepsilon_0/\sigma_0 \approx 440$ s can be considered to be quasi-steady. Here, $\varepsilon_0 \approx 8.854 \times 10^{-12}$ F/m is the permittivity of vacuum and $\sigma_0 = 2 \times 10^{-14}$ S/m is the air conductivity at the oceanic surface under undisturbed conditions. Since the conductivity increases nearly exponentially with altitude at a rate governed by a scale height of 2–3 km, the characteristic time decreases by up to two orders of magnitude, i.e., to a few seconds, at heights occupied by the typhoon.

In accordance with [5,6], the following relation can be obtained for estimating the cyclone-induced electric field in the ionosphere:

$$E_i = \frac{j_a}{\sigma_i},$$

where $\sigma_i \approx 10^{-6}$ S/m is the plasma conductivity at the lower boundary of the ionosphere. Inserting the value of j_a estimated above into this relation yields $E_i \approx 3$–30 mV/m. These values of E_i exceed the background value of the ionospheric electric field by 1–2 orders of magnitude.

It should be noted that the medium above the lower boundary of the ionosphere becomes considerably anisotropic, acting to change the polarization of the electric field penetrating the ionosphere. The electric field component directed perpendicular to the geomagnetic field becomes predominant, and consequently, the Pedersen conductivity, which is significantly smaller than the parallel conductivity, maximizes. As a result, an ionospheric electric field strength is estimated to be 5 mV/m for the electric current density of 10^{-7} A/m^2.

It should be noted that this field is a maximum not strictly above the TC (typhoon) but somewhat away from it because the disturbances are transported along the geomagnetic field lines from the ionospheric E-region dynamo heights ($z \sim 100$–150 km) to the higher

altitudes along the geomagnetic field lines, resulting in a disturbance lateral displacement. The magnitude of the displacement attains 600–800 km [5,6], which is of the same order of magnitude as the scale size of the meteorological object.

To date, discussions are ongoing on whether the electric fields can penetrate the ionosphere deep or not. Some researchers believe that they cannot [89–96], while others give an affirmative answer [5,6,8]. Both may be right. The fact is that an electrostatic field really cannot penetrate deep into the ionosphere; it is weakened by many orders of magnitude below the ionosphere. An alternating electric field penetrates the ionosphere quite deeply. There are a few reasons for this. First, the electric current density in the atmosphere above a typhoon increases by a few orders of magnitude, attaining 10^{-7} A/m^2. Second, it can be shown that the skin depth is given by

$$l_E = 2H_\sigma \ln\left(\frac{c}{H_\sigma}\sqrt{\frac{T_E t_0}{\pi}}\right),$$

where H_σ is the characteristic scale length of the exponential relation for atmospheric conductivity increasing with height, T_E is an electric field characteristic time scale, and t_0 is the value at the Earth's surface.

Then for characteristic times of 10^{-3}–10^3 s, the skin depth is equal to or exceeds 60–110 km, which allows the penetration of the electric fields without significant damping into the ionosphere, i.e., into the medium with a high conductivity. And finally, the fact that the electric field is quasi-static, or more precisely, alternating with characteristic times of hundredths of a second to thousands of seconds, is of fundamental importance. It can be shown that this time scale is established by turbulent processes operating within the typhoon. For the characteristic time of 0.1 s and the electric field fluctuations of the order of 10–100 V/m in thunderstorm clouds within the typhoon, we have the displacement current of the order of 10^{-9}–10^{-8} A/m^2 in the Earth–ionosphere cavity. For the electrical conductivity of 10^{-6} Ohm^{-1} m^{-1} at the lower boundary of the ionosphere, we obtain the electric field strength of the order of 10^{-3}–10^{-2} V/m in the lower ionosphere.

The possibility of penetration of quasi-static (but not static) electric fields is confirmed by satellite observations [5–7,97] and by detailed calculations [8].

Thus, there are physical reasons for the penetration of quasi-stationary fields from the typhoon to ionospheric heights.

11.4. Generation of Magnetic Fields

The enhancement of the atmospheric electric current flow in the vicinity of a TC (typhoon) acts to create disturbances in the geomagnetic field. The TC (typhoon) can be approximated by a right vertical cylinder of radius R_0. The circumference of the volume with the electric currents is equal to $2\pi R_0$, and the surface area of the cylinder cross section is $S_0 = \pi R_0^2$. Ampère's law for the magnetic induction can be cast in the following form:

$$\oint \mathbf{B} \cdot d\mathbf{l} = \mu_0 \int \mathbf{j} \cdot d\mathbf{S}.$$

Then the change ΔB in the magnetic induction is given by the relation

$$\Delta B(R_0) = \frac{1}{2}\mu_0 j_a R_0.$$

For example, at $j_a \approx 3 \times 10^{-9}$ A/m^2, R_0 = 600 km, we obtain $\Delta B(R_0) \approx 1.1$ nT. The $\Delta B(R_0)$ estimates are presented in Table 9.

Table 9. Electrical parameters of TC (typhoon) vs. electric charge density. Here, E_e is the electric field strength within a cloud, F_e, F_p, F_k, and F_c are specific electrostatic, thermodynamic, Coriolis, and centripetal forces, respectively; in addition, $F_e = QE_e$, $F_p = \Delta p(r_0)/r_0$, $F_k = 2\omega v_0 \rho$, and $F_c = \rho v_0^2/2$.

Variables	Values					
Q (C/m^3)	10^{-10}	10^{-9}	10^{-8}	10^{-7}	10^{-6}	10^{-5}
w_0 (m/s)	3×10^{-2}	4×10^{-2}	5×10^{-2}	0.1	0.2	0.3
j_a (A/m^2)	3×10^{-12}	4×10^{-11}	5×10^{-10}	10^{-8}	2×10^{-7}	3×10^{-6}
$\dot{Q}$ (A/m^3)	3×10^{-16}	4×10^{-15}	5×10^{-14}	10^{-12}	2×10^{-11}	3×10^{-10}
E_e (V/m)	10^5	2×10^5	4×10^5	6×10^5	8×10^5	10^6
F_e (N/m^3)	10^{-5}	2×10^{-4}	4×10^{-3}	6×10^{-2}	0.8	10
F_p (N/m^3)	0.1	0.3	0.6	0.8	1.1	1.2
F_k (N/m^3)	2×10^{-3}	4×10^{-3}	7×10^{-3}	8×10^{-3}	9×10^{-3}	10^{-2}
F_c (N/m^3)	3×10^{-2}	0.1	0.2	0.3	0.4	0.5
v_0(m/s)	15	30	50	60	70	80
r_0 (km)	10	11	14	15	16	18
$\Delta p(r_0)$ (kPa)	0.8	3	9	12	17	22
R_0 (km)	400	450	570	610	650	700
$\Delta B(R_0)$ (nT)	7.5×10^{-4}	1.1×10^{-2}	0.2	3.8	82	1.3×10^3

11.5. Impact on Energetic Particles

The typhoon-induced quasi-steady electric fields are mapped, insignificantly weakening, along geomagnetic field lines to the magnetosphere and under certain conditions reduce the perpendicular component of energetic particle energy by a value of $\varepsilon_\perp = eE_iL_\perp$ where $L_\perp$ is the horizontal extent of electric field perturbations. Assuming $L_\perp = 2R_0 \approx 1000$ km, E_i = 3–30 mV/m, we obtain $\varepsilon_\perp \approx$ 5–50 keV. Such values of $\varepsilon_\perp$ are enough to redistribute the particles over pitch angles and to cause particle precipitation from the radiation belts into the upper atmosphere, as well as to launch the secondary processes already mentioned above.

12. Observations

The multifrequency multiple path radio system has been used to observe the ionospheric response to typhoons at oblique incidence [10–13]. The schematic presentation of the HF great-circle propagation paths is presented in Figure 1.

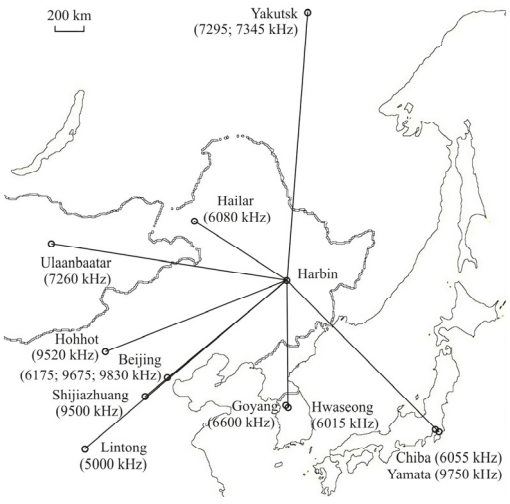

Figure 1. Schematic presentation of the great-circle propagation paths used for the observation of the ionospheric response to typhoons.

The ionospheric response to a few unique typhoons is described in the works by [10–13]. The basic information on the typhoons is shown in Table 10.

Table 10. Basic information on the typhoons.

Typhoon Parameter	Kong-Rey	Lekima	Lingling	Faxai	Hagibis
Birth	29 September 2018 06:00:00 UTC	4 August 2019 06:00:00 UTC	2 September 2019 00:00:00 UTC	4 September 2019 18:00:00 UTC	5 October 2019 18:00:00 UTC
Death	6 October 2018 12:00:00 UTC	12 August 2019 18:00:00 UTC	8 September 2019 00:00:00 UTC	10 September 2019 00:00:00 UTC	13 October 2019 03:00:00 UTC
Lifetime	174 h/7.250 days	204 h/8.500 days	168 h/7.000 days	126 h/5.250 days	177 h/7.375 days
Minimum pressure	900 hPa	925 hPa	940 hPa	955 hPa	915 hPa
Pressure maximum deficit	105 hPa	75 hPa	65 hPa	52 hPa	95 hPa
Maximum wind speed	215 km/h (60 m/s)	195 km/h (54 m/s)	176 km/h (49 m/s)	157 km/h (43.7 m/s)	259 km/h (71.8 m/s)
Largest radius of storm wind	260 km	190 km	170 km	110 km	370 km
Largest radius of gale wind	750 km	700 km	560 km	330 km	750 km
Length of movement	4107 km	2854 km	3750 km	3663 km	4785 km
Average speed	23.6 km/h (6.56 m/s)	14.0 km/h (3.9 m/s)	26.0 km/h (7.2 m/s)	29.1 km/h (8.1 m/s)	27.0 km/h (7.5 m/s)
Range of movement	Latitude 25.3°; Longitude 16.7°	Latitude 21.0°; Longitude 11.1°	Latitude 29.2°; Longitude 4.6°	Latitude 20.4°; Longitude 17.8°	Latitude 25.8°; Longitude 20.4°
Typhoon kinetic energy	1.65×10^{18} J	7.8×10^{17} J	5.5×10^{17} J	1.8×10^{17} J	5.5×10^{18} J
Typhoon power	1.7×10^{13} W	4.6×10^{12} W	5.5×10^{12} W	1.3×10^{12} W	1.1×10^{14} W
Rainfall	250–300 mm h^{-1}	250–300 mm/h	250–320 mm/h	260–300 mm/h	260–300 mm/h
Maximum pressure drop	−25 hPa/6 h; −40 hPa/12 h −65 hPa/24 h; −96 hPa/48 h	−10 hPa/6 h; −20 hPa/12 h −35 hPa/24 h; −50 hPa/48 h	−10 hPa/6 h −15 hPa/12 h −30 hPa/24 h −50 hPa/48 h	−10 hPa/6 h −15 hPa/12 h −25 hPa/24 h −39 hPa/48 h	−15 hPa/6 h −30 hPa/12 h −60 hPa/24 h −85 hPa/48 h

In the discussion below, we present the illustrations of typhoon-induced variations in the radio wave characteristics and ionospheric parameters.

12.1. Ionospheric Disturbances That Accompanied the Super Typhoon Kong-Rey Event of September–October 2018 over China

The ionospheric effects from super typhoon Kong-Rey for twelve radio paths are described in detail in [13]. In this section, as an illustration, the observations along the Hwaseong–Harbin radio-wave propagation path are presented. This radio station, operating at 6015 kHz during the 03:00–24:00 UTC period, is located at the City of Hwaseong, the Republic of Korea, at a great-circle distance of 950 km from the City of Harbin.

The radio wave at such a low frequency reflects from the ionosphere at *E*-region heights during sunlit hours and at *F*-region heights during the night. This is the reason for the features of the variations in Doppler shift that can be seen in Figure 2. The 29 and 30 September 2018 period was used as a quiet time reference when the Doppler shift exhibited variability within the ±(0.2–0.3) Hz limits and, from time to time, showed quasi-periodic variations with ~0.1–0.2 Hz amplitudes, f_{Da}, and ~20–30 min periods, T.

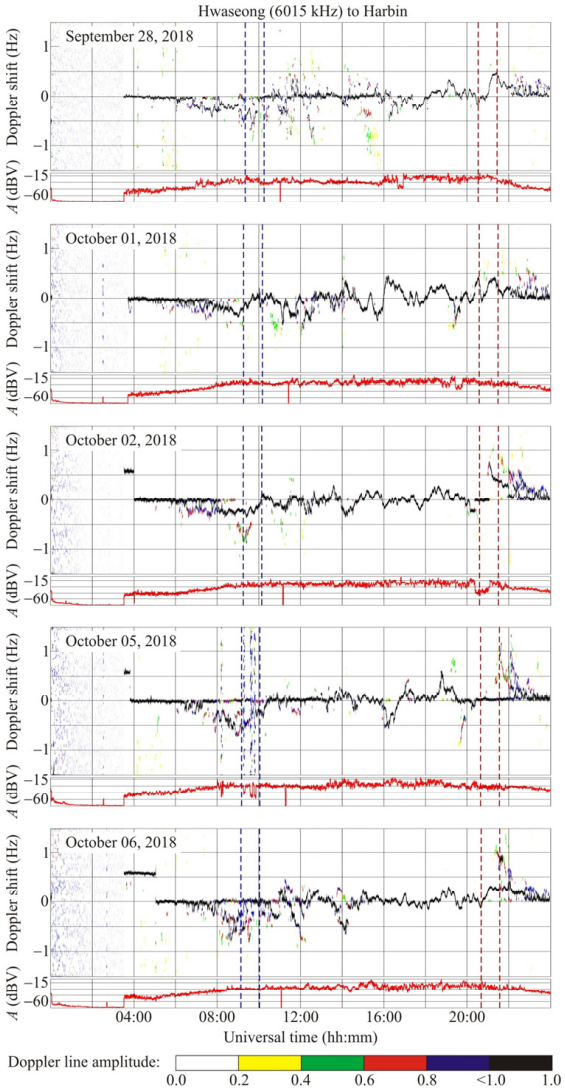

Figure 2. Universal time variations of the Doppler spectra along the Hwaseong–Harbin propagation path for 28 September, and 1, 2, 5, and 6 October 2018 (panels from top to bottom, respectively). The radio wave frequency is 6015 kHz. The black, blue, red, green, and yellow colors show the Doppler line amplitude of 1, 0.8, 0.6, 0.4, and 0.2 on a relative scale, respectively. The Doppler shift plot comprises 117,600 points in every 1 h interval. Vertical dashed lines indicate the sunsets (two left-hand blue lines) and sunrises (two right-hand red lines) at 0 and 100 km altitude. The signal amplitude, A, at the receiver output in decibels, dBV, relative to 1 V is shown below the Doppler spectrum in every panel.

At nighttime on 1 October 2018, the Doppler shift quasi-periodic variability was notably enhanced, with $f_{Da} \approx 0.3$–0.5 Hz and $T \approx 20$–120 min, when the midpoint of the Hwaseong–Harbin propagation path was found within the ~2800–3300 km range from the typhoon. Similar effects were also observed over the propagation paths Chiba/Nagara–Harbin, Goyang–Harbin, and Yamata–Harbin closest to the typhoon, whereas a similar effect was not recorded along the remote Hohhot–Harbin propagation path.

On 2 October 2018, typhoon Kong-Rey approached the shortest distance from the propagation paths being employed, which was close to 600 km. However, the typhoon had already reduced its intensity by a factor of 2, which resulted in the reduction of the ionospheric response to the typhoon Kong-Rey movement ($f_{Da} \approx 0.1$–0.3 Hz, $T \approx 20$–80 min).

On 3 and 4 October 2018, the variations in Doppler shift did not exceed 0.2 Hz, with one exception that the Doppler shift amplitude attained 0.5 Hz on 3 October 2018, while quasi-periodic perturbations were practically absent during this period.

The Doppler shift showed, on the contrary, sign–ficant variations, from −(0.5–0.7) Hz to 0.5–0.6 Hz, with $f_{Da} \approx 0.1$ Hz and $T \approx 20$–30 min on 5 and 6 October 2018. Moreover, Typhoon Kong-Rey was at 1000–1500 km from the propagation path midpoint and reduced its intensity by a factor of 3 compared with its initial intensity.

The use of a large number of radio wave propagation paths permitted the direction and average speed of the 60–70 min period wave perturbations propagating from the typhoon to be determined to be 205 ± 6 m/s, which pertain to the atmospheric gravity waves.

12.2. Ionospheric Disturbances That Accompanied the Super Typhoon Lekima Event of 4–12 August 2019

The ionospheric effects of Typhoon Lekima are described in detail in [12]. Figure 3 shows that Doppler spectrum spreading was observed to occur throughout the 6–10 August 2019 period. The Doppler shift showed considerable variations on the nights of 6/7 and 10/11 August 2019 (the night of 7/8 is not shown). Moreover, the temporal variations in the Doppler shift exhibited a quasi-periodic variation with a 12–15 min period and $f_{Da} \approx 0.10$–0.15 Hz amplitude, while the signal amplitude exhibited variability within the −45 dBV to −15 dBV limits.

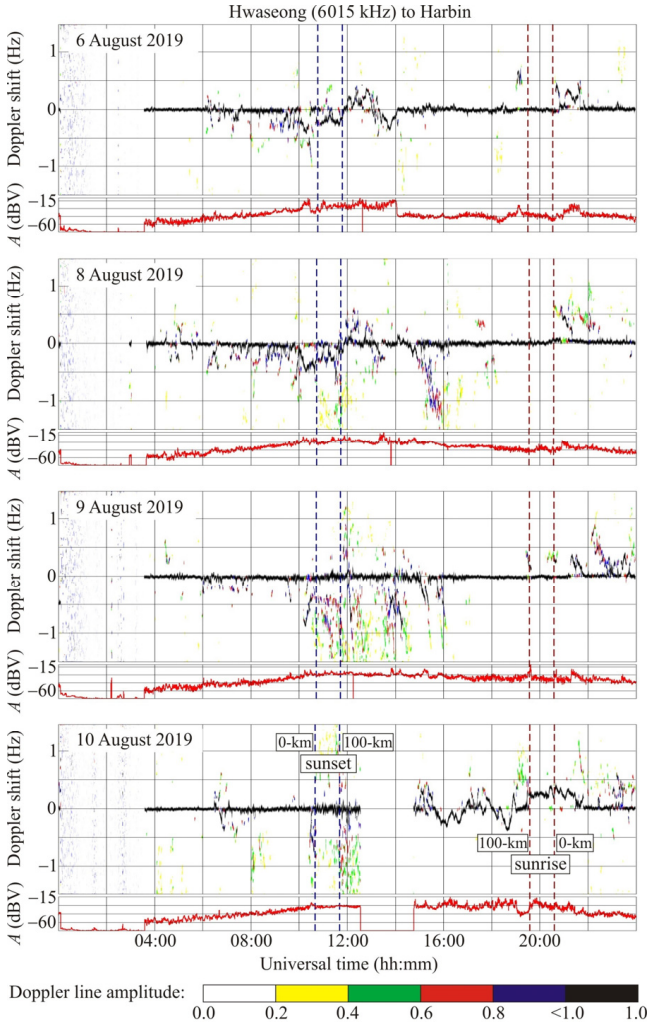

Figure 3. Same as in Figure 2 but for the super typhoon Lekima.

12.2.1. Doppler Spectrum Variations

Along most of the propagation paths, the variations in the Doppler spectra were the most pronounced on 6, 8, and 10 August 2019. Even though the typhoon was situated far away from the propagation paths on 6 August 2019, its power was approximately a maximum (~10^{13} W), and it could produce observable perturbations. The variations that were observed on that day were unlikely to be due to other sources, such as the terminator or the magnetic storm commencement on 5 August 2019. The super typhoon energy attained a maximum value on 8 August 2019, and the variations in the Doppler spectra could be considered to be due to its action. On 10 August 2019, the super typhoon energy was smaller than that on 8 August 2019 by a factor of 2.5 to 3. Nevertheless, at that time, the typhoon reached the coastline of the People's Republic of China, and for this reason, the variations in the Doppler spectra could be due to the action of this typhoon. In addition, the typhoon pressure on 7 and 9 August 2019 varied weakly. This is apparently the cause of the lack of ionospheric response. The fact that the magnitude of the effects observed decreased with increasing distance between the typhoon and the propagation path midpoints supports the assumption that the variations detected in the Doppler spectra on 8 and 10 August 2019 were associated with the typhoon. This assertion is true for the Hohhot–Harbin, Ulaanbaatar–Harbin, and Yakutsk–Harbin propagation paths. Along the Hwaseong–Harbin and Goyang–Harbin propagation paths, this effect displays itself more clearly. Thus, a spreading of the Doppler spectra and an increase in the amplitude of the Doppler shift suggest an enhancement in wave activity at ionospheric heights.

12.2.2. Amplitude Effect

Considerable variations in the Doppler spectra were usually associated with significant changes in the amplitude of the signals. The amplitude effect was pronounced to a greater degree along the Lintong/Pucheng–Harbin, Shijiazhuang–Harbin, Hwaseong–Harbin, Hohhot–Harbin, and Yakutsk–Harbin propagation paths. In a few cases, the amplitude of the signals varied quasi-periodically.

The results may be summarized as follows. The maximum disturbance in the ionosphere was observed during the day the super typhoon Lekima's energy was at a maximum and during the day the super typhoon came close to the middle of each radio-wave propagation path. The magnitude of the ionospheric perturbations decreased with the distance between the super typhoon and the propagation path midpoints. Both aperiodic (chaotic) and quasi-periodic disturbances accompanied the super typhoon action in the ionosphere. The periods of the quasi-periodic disturbances were estimated to be ~12–24 min, which pertain to atmospheric gravity waves. The atmospheric gravity waves launched by the super typhoon gave rise to quasi-periodic variations in the electron density with amplitudes of ~3% to ~19%.

12.3. Ionospheric Disturbances That Accompanied Typhoon Activity in the Vicinity of China in September 2019

The ionospheric effects that accompanied the action of two typhoons are described in detail in [11]. Figure 4 shows that the most significant variations in the Doppler spectra were captured on 6 and 9 September 2019. In this case, the Doppler spectrum spreading reached ±1.5 Hz. On 7 (not shown), 8, and 10 September 2019, the spreading was significant but did not exceed ±0.5 Hz. In addition to chaotic variations in the Doppler shift, their quasi-periodic changes were also recorded. In this case, the period ranged from 17–20 min to 30–60 min, and $f_{Da} \approx 0.2$–0.3 Hz.

The amplitude of the signal also fluctuated according to aperiodic and quasi-periodic laws. In this case, $T \approx 30$–40 min, and the oscillation amplitude was about 5 dBV.

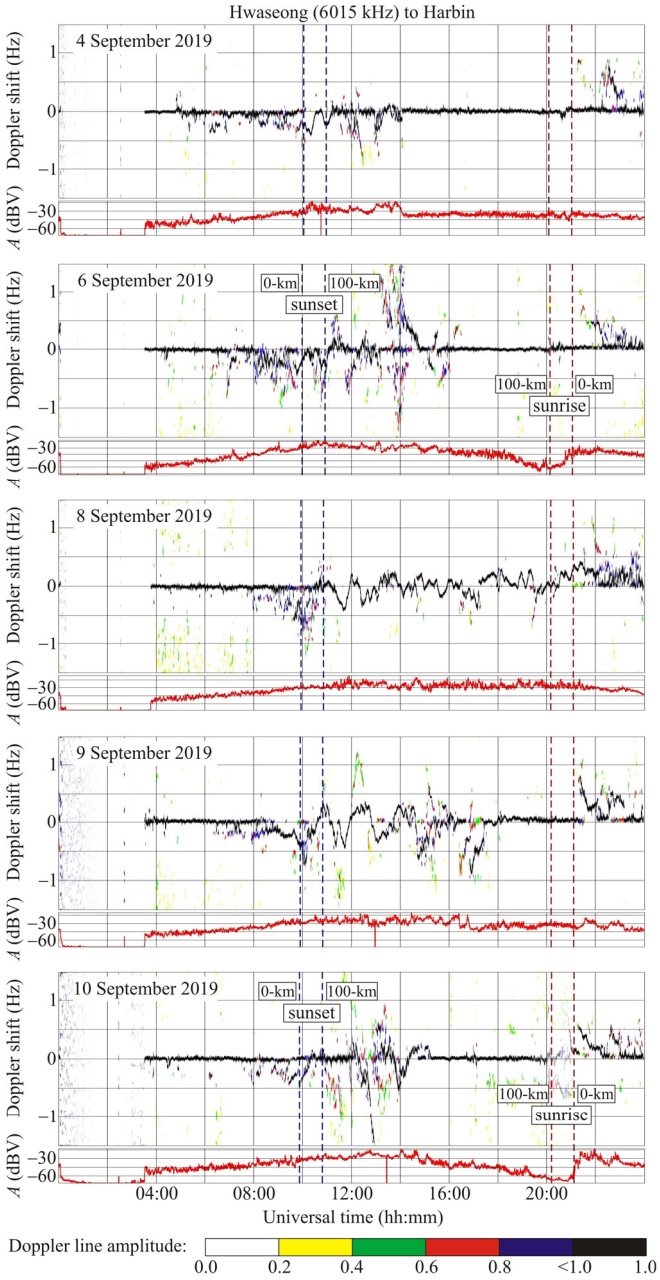

Figure 4. Same as in Figure 2 but for the typhoons Lingling and Faxai.

Ionospheric Response to Typhoons

Typhoon Lingling was most active on 5 September 2019. Its activity was also high on the previous and the following day, 4 and 6 September 2019. From 4 to 6 September 2019, the typhoon was located at considerable (at least 1400–1500 km) distances from the midpoints of the nearest radio propagation paths. The latter include the Hwaseong–Harbin, Goyang–Harbin, Chiba–Harbin, and Yamata–Harbin propagation paths. Over three of these propagation paths (except for the Goyang–Harbin radio propagation path), significant variations in the Doppler spectra occurred on 6 September 2019. Along other radio propagation paths, the influence of Lingling typhoon was not observed confidently.

On 6 September 2019, the Doppler spectra along the Hwaseong–Harbin and Chiba–Harbin propagation paths exhibited considerable (from −1.5 Hz to 1.5 Hz) spreading and diffuseness. The latter was caused by plasma turbulence in the ionosphere. The Doppler shift over the Yamata–Harbin radio propagation path on 6 September 2019 was fairly regular and had a pronounced quasi-periodicity with $T \approx 50$ min, $f_{Da} \approx 0.2$–0.5 Hz.

Typhoon Faxai was closest to Japan and PRC on 9 September 2019. The typhoon was not too far from these countries on adjacent days, 8 and 10 September 2019. Indeed, significant variations in the Doppler spectra on 9 September 2019 were observed along all propagation paths with an acceptable operating mode (the Beijing–Harbin radio propagation path at $f \approx 9675$ kHz turned out to be not suitable for analyzing the dynamics of the ionosphere). Significant variations in the Doppler spectra during 8 September 2019 were observed over 9 out of 10 propagation paths (with the exception of the remote Ulaanbaatar–Harbin radio propagation path), and on 10 September 2019, along 8 out of 9 radio propagation paths. Over the Hohhot–Harbin radio propagation path, there were no noticeable changes in the Doppler spectra.

The main manifestations of the typhoon's impact on radio wave characteristics are as follows. Considerable Doppler spectrum variations were absent on the reference days.

Significant variations were observed only in the three nearest to Lingling typhoon radio propagation paths and only on 6 September 2019 when the typhoon was already weakening. There were no signs of the typhoon on more distant radio propagation paths.

Significant variations in the Doppler spectra on 9 September 2019 were observed along all 10 out of 10 propagation paths suitable for analysis; on 8 September 2019, the Doppler spectrum variations were observed over 9 out of 10 propagation paths (the response to the typhoon was not recorded for the most remote radio propagation path Ulaanbaatar–Harbin), and on 10 September 2019, variations were observed along 8 of 9 radio wave paths. This means that the increasing distance of Typhoon Faxai from the radio propagation path midpoints and its smaller energy on 10 September 2019 resulted in a decrease in the ionospheric response.

We summarize the main results as follows. On 6 September 2019, the ionospheric response to Typhoon Lingling was detected on three adjacent radio propagation paths. Chaotic and quasi-periodic variations of the Doppler shift were observed along with a significant expansion (from -1 Hz to 1 Hz or greater) of the Doppler spectra. The response to Typhoon Lingling was observed during the weakening stage when the atmospheric pressure deficit was between 35 and 55 hPa; at the same time, the typhoon approached as close as possible for the observing instruments to the radio propagation paths and remained quite strong. The ionospheric response to Typhoon Faxai was clearly observed on 8–10 September 2019 as the typhoon approached the middle of the radio propagation paths. It is important that the response was observed on all or most of the radio propagation paths. As the typhoon moved away from the middle of the radio paths, the magnitude of the response diminished. The chaotic variations of the Doppler spectra were caused by the generation of plasma turbulence at the ionospheric levels by typhoons. The quasi-periodic variations of the Doppler shift in the main ray are caused by atmospheric gravity waves and infrasound generated by typhoons. The amplitude of quasi-periodic variations in the concentration of electrons in the field of infrasound waves reached several percent, and in the field of atmospheric gravity waves, it attained from ten to several tens of percent. Quasi-periodic variations in the signal amplitude are caused by focusing and defocusing the radio beam in the field of the atmospheric gravity wave. The aperiodic variations in the signal amplitude are due to the statistical diffraction of the radio waves around spatial inhomogeneity that arises (or amplifies) under the influence of typhoons. The effect of Typhoon Lingling at night on 6 September 2019 was accompanied by a 23% reduction in electron concentration in the *F*-region of the ionosphere. The action of Typhoon Faxai at night on 9/10 September 2019 was accompanied by a decrease in the electron concentration in the *E*- and *F*-regions of the ionosphere by 27%. With the maximum approach of Typhoon Faxai to the ionosonde at nighttime on 8 September 2019 when the typhoon had the highest energy, an increase of 56% was noted in the electron concentration in the *F*-region of the ionosphere.

12.4. Ionospheric Disturbances That Accompanied the Super Typhoon Hagibis Event of 6–13 October 2019

The response of the ionosphere to the impact of Typhoon Hagibis along eleven radio wave paths is described in [10]. Figure 5, for the Hwaseong–Harbin radio wave propagation path, shows that the $f_D \approx 0$ Hz, and $A \approx -45$ dBV during sunlit hours every day. Near dusk, the Doppler shift gradually decreases from 0 Hz to −(0.3–0.4) Hz, and the Doppler spectra spread very little.

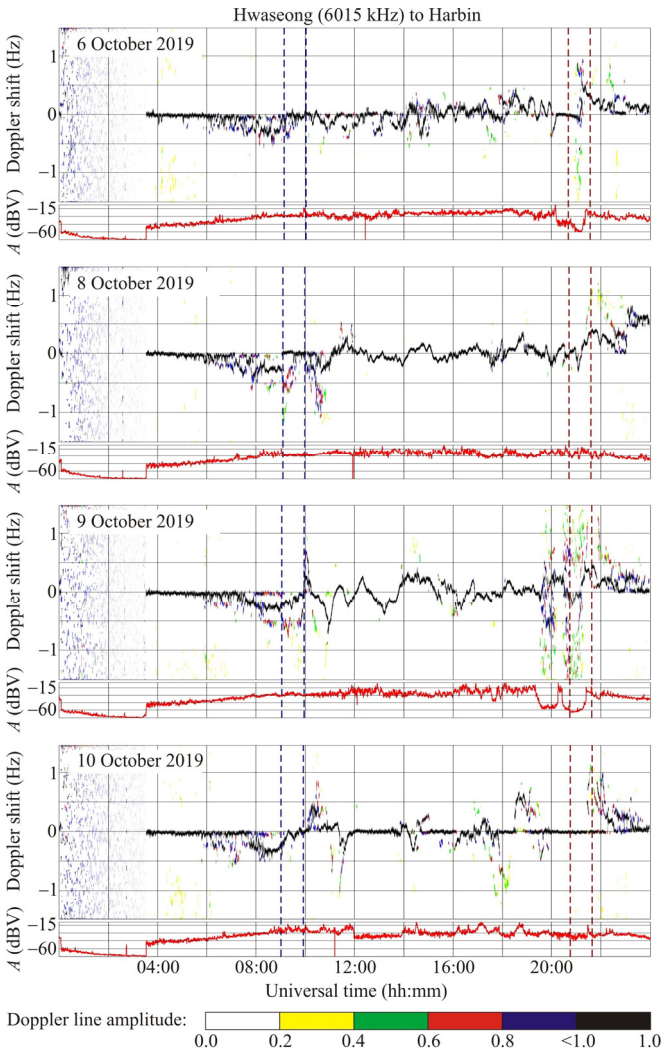

Figure 5. Same as in Figure 2 but for Typhoon Hagibis.

In the course of all the nights, the Doppler shift varied strongly, $f_{Da} \approx 0.2$–0.4 Hz. Generally, the Doppler shift changed quasi-periodically with ~20–80 min period, T, and ~0.1–0.3 Hz amplitude, f_{Da}.

The greatest variations in the Doppler shift were observed on 7, 8, 9, 11, and 12 October 2019. In addition, an oscillation with an ~15 min period, T, and ~0.05–0.10 Hz amplitude, f_{Da}, was recorded on 12 October 2019.

The smallest variations of ~0.1–0.2 Hz in the Doppler shift were detected on 13 October 2019.

The amplitude, $A(t)$, of the signal exhibited the greatest variations at nighttime on 10 and 11 October 2019.

On 12 October 2019, the super typhoon was at the shortest distance from Japan and the radio wave propagation paths; however, the level of its activity considerably diminished at that time, i.e., the pressure deficit was lower than 20–40 hPa and the winds became slower,

90–120 km/h or 20–33 m/s. Therefore, the super typhoon could not have a significant effect on the ionosphere.

The variability of the Doppler spectra along all propagation paths was maximum on 9 October 2019, whereas the variations were relatively smaller on 8 and 10 October 2019. Over the 8–10 October 2019 period, the super typhoon accumulated the highest energy, i.e., the pressure maximum deficit attained about 95 hPa and the maximum wind speeds of 250–260 km/h or 69–72 m/s. On 9 October 2019, the distance between the super typhoon and the propagation path midpoints was found to be ~2500–3000 km.

It is important that analogous variations on 6, 7, 11, 12, and 13 October 2019 used as a quiet time reference were absent or considerably smaller than on 8 or 10 October 2019 and especially on 9 October 2019.

It should be noted that wave perturbations may happen without tropical cyclones or typhoons, which can be seen in the observations made on quiet time reference days and presented in [10]. The authors argue that typhoons generally act to enhance wave activity, and this can also be seen in the data averaged over 28 reference days in October 2019 when the Doppler shift was estimated to be 0.21 $\pm$ 0.02 vs. 0.53 $\pm$ 0.04 Hz on 9 October 2019 [10].

The authors [10] summarize the main results as follows. The action of the super typhoon was accompanied by enhanced wave activity in the atmosphere acting to generate wave processes with periods of 12–15 min to 60–150 min. Coupling in the atmosphere–upper-atmosphere–ionosphere system has been confirmed to be carried out with the atmospheric gravity waves. The ionosphere underwent the greatest impact on the days the super typhoon had maximum energy—on 8, 10, and especially 9 October 2019—and the super typhoon was found to be in the ~2500–3000 km distance range from the propagation path midpoints. Under the action of wave processes on 9 October 2019, the height of the reflection level was observed to oscillate within the 30–50 km to 60–90 km limits. The amplitude of the quasi-periodic variations in the ionospheric *F*-region electron density was estimated to be 10–12% for periods of ~20 min, and 30–60% for periods of ~60–120 min. The joint action of the dusk terminator and the super typhoon was confirmed to enhance wave activity in the ionosphere. Similar effects for the dawn terminator were not detected. Manifestations of infrasonic oscillations in the ionosphere were detected. The period of the infrasound changed from 2 min to 7 min, depending on the altitude of the sounding. The amplitude of the quasi-periodic variations in the electron density varied in the 0.2–0.4% range. Synchronous quasi-periodic variations in the signal amplitude were detected with a peak-to-peak amplitude of 10 dBV and a period of 7 min; these variations arise from radio ray focusing/defocusing caused by the quasi-periodic electron density variations produced by the action of infrasonic waves. The variations in the critical frequency of the F_2 layer that could be due to the action of the typhoon were detected.

13. Discussion

The influence of atmospheric processes on the upper atmosphere has long been suspected to exist; however, definite proof has been given only lately (see, e.g., [5,6,10–13,79]). Extratropical cyclones always exist, which means that their impact on the upper atmosphere may be regular. The difference between TCs and extratropical cyclones is in the ocean–lower atmosphere coupling. Thus, the role that a TC plays in the ocean–atmosphere–ionosphere–magnetosphere becomes significant. In the present paper, the model of a coupling between the subsystems listed above is presented schematically. Some processes are treated in more detail while others only schematically.

The study of the coupling between the ocean and TCs was given enough details (see, e.g., [67,71,98]). The work [9] is interesting in that it deals with nonlinear coupling in the ocean–TC subsystem and shows that this process can be described by damped nonlinear oscillations under conditions of a steady TC, which rarely happens, whereas this work accounts for the TC movement as well. In addition, we make a natural assumption that the energy in the emerged cyclone is replenished till the oceanic surface layer temperature, t_1, exceeds the temperature t_{1m} of the cool lower layers of the ocean, while the $t_1 > t_c$

condition is assumed to be sufficient for the replenishment to occur. Since $t_c \approx 26.5$ °C and $t_{1m} \approx 23$ °C, then the difference is significant. In particular, the steady value $t_s < t_c$ in our case. In addition, the steady value of the tangential component in the spiral of the speed in the cyclone can attain 50–60 m/s, whereas it was assumed to be about 20 m/s in [9], although a value of $v_0 \approx 20$ m/s is too small for hurricanes (typhoons).

We consider the following three mechanisms affecting the upper atmosphere and geospace by TCs: acoustic–gravity waves, electromagnetic waves, and quasi-steady electric fields. The AGW energy fluxes have been calculated. Even for the greatest hurricanes and typhoons, the IGW power P_r is shown to be considerably—two orders of magnitude—smaller than the power P_f produced by friction between the cyclone and the oceanic surface. Taking into account that P_f is proportional to v_0^3, whereas P_r is proportional to $v_0^{53/12}$, a conclusion may be drawn that the enhancement in the wind speed in the hurricane (typhoon) and an increase in the maximum power associated with air fluxes would be inhibited by the generation of IGWs. However, this would occur at unrealistically large values ofv_0.

The power of IGW radiation for the most violent typhoons attains 10^{11}–10^{12} W. As a comparison, the IGW power radiated by all mountain ranges on the planet (orographic waves) is estimated to be 10^{11} W on average.

There are two possible generation mechanisms of magnetic perturbations by IGWs. The first involves the modulation of the ionospheric currents, and the second mechanism is due to the IGW drag on charged particles, with the contribution from the second process being a factor of 5–10 times more efficient.

An interesting conclusion of this study is the opportunity to generate disturbances in the geomagnetic field not only at the IGW frequency, which is natural, but also at a doubled frequency due to gas heating by IGWs dissipating their energy at 80–200 km heights, where a wave-medium nonlinear interaction plays a major role. We can estimate the time delay of the geomagnetic field variations that occur at twice the frequency of oscillations in atmospheric pressure at the ground. Suppose that an IGW, with a period of 1 h, travels to the upper atmosphere at a speed close to 0.2 c_{s0} [79], then the propagation delay to reach an altitude of ~120 km is approximately 30 min. The time delay of temperature variations associated with the gas heating is $T_w/4 \approx 25$–30 min (see (41) and (46)). Thus, the total time delay should be approximately 55–60 min. Finally, we have explained the result of [79] where the most probable IGW period is estimated to be 1.5 h. The radiation intensity is shown above to exhibit a sharp increase in the vicinity of the frequency Ω_1, which corresponds to a period of $T_{r1} \approx 1.45$ h (at turbulent pulsations in the speed of $\widetilde{v} \approx 6$ m/s and vortex radius of $l \approx 500$ km). It should be noted that AGWs were observed to be generated not by a TC but by a powerful weather front [79]. The difference lies in the mechanisms for forming atmospheric vortexes, while the mechanisms for generating AGWs remain analogous to each other because they are due to an enhancement in atmospheric turbulence in both cases.

At 100–150 km altitude where the speed v_w is comparable in magnitude with the speed of sound, the IGWs become nonlinear, which leads to energy dissipation and the emergence of a range of dynamic and thermal effects. They include rising heated air parcels, the excitation of hydrodynamic instabilities in the atmosphere, an enhancement in turbulence, the formation of a jet stream [81] and dissipating structures, AGW instability induced by significant enhancements in electric fields at ionospheric heights, the formation of AGW vortices, etc. [82].

The electromagnetic radiation from TCs is due to thunderstorms occurring at the cyclone core. The lightning-induced VLF radio waves are transmitted into the magnetosphere where they interact with the trapped particles and cause precipitation of relativistic electrons. The processes occurring in the geomagnetic flux tube were studied in detail by [99]. The estimate of the trigger effect was performed by the author of this paper.

The mechanisms for the perturbation of quasi-steady electric fields and the results of corresponding observations are discussed by [5,6] who do not indicate the causes of an enhancement in the electric currents at the ocean–atmosphere interface. Apparently,

the growth of the electric currents is due to an increase in the aerosol production and electrification rates as a result of significant enhancements of the wind within a developed cyclone.

Finally, it should be noted that the role that the electrical processes play in TCs has been underestimated until now. The author's attention is drawn to the need to take them into account [1]. Calculations show that the electric forces can be not only significant but also decisive (Table 9). The latter can arise in the cyclone only if $Q \geq 10^{-6}$ C/m^3 and $j_a \geq 10^{-7}$ A/m^2. In this case, the TC (typhoon) impact on the ionosphere and magnetosphere should also increase since $j_a/j_{a0} \geq 10^5$. At a great enough charge density Q, the air within a TC (typhoon) behaves like a magnetized plasma. In such a medium, vortexes of electromagnetic nature, low-frequency waves, electrical structures, instabilities, etc., can be expected to appear. New channels for a cyclone's impact on the ionosphere and magnetosphere arise as a result of the evolution of such processes. Serious consideration, however, needs to be given to these issues.

Thus, a schematic model for processes acting in the ocean–cyclone–upper-atmosphere–ionosphere–magnetosphere system has been developed in this work for the first time (Figure 6). The main key aspects of coupling between the subsystems are based on the observations made by a number of researchers. Certainly, this model will be developed in the future to describe the internal workings of the coupled system in more detail.

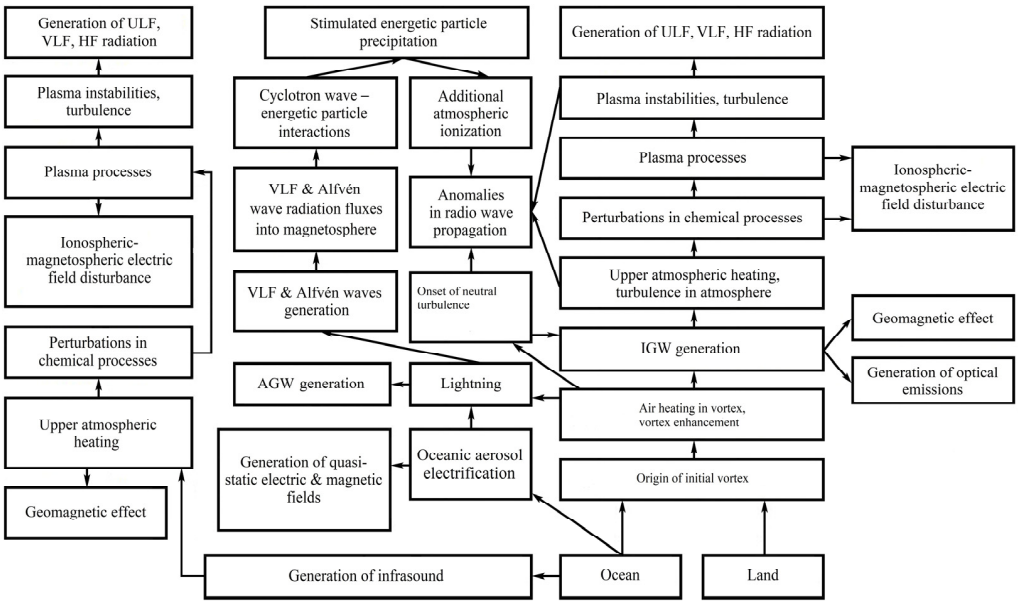

Figure 6. Block diagram of the processes in the ocean–atmosphere–ionosphere–magnetosphere system.

14. Conclusions

1. The premise has been validated that a tropical cyclone (typhoon, hurricane), one of the most powerful large-scale formations systematically arising in the atmosphere, is an element of the ocean–atmosphere–ionosphere–magnetosphere system. The TC plays a crucial role with regard to global-scale mass and energy exchange in this system.
2. The study of this system encompasses a broad spectrum of physical phenomena occurring and processes operating within the system components, as well as the mechanisms for their interactions. The problem under discussion is interdisciplinary. It ranges from different Earth sciences to geospace sciences, which comprise the physics of the ocean, meteorology, the physics of the Earth's atmospheric and space environment, geomagnetism, etc.
3. The foundations of a schematic model for the main processes operating in the ocean–atmosphere–ionosphere–magnetosphere system have been built.

4. The subsystems and the system as a whole demonstrate nonlinearity. This produces nontrivial properties of the system such as the excitation of instabilities, the emergence of self-organization, trigger mechanism working, etc.
5. The main mechanisms for coupling the subsystems are indicated. The feedback and coupling processes operate between the subsystems. It is important that these processes are characterized by significant energetics, which leads to the nonlinearity of the main physical processes.
6. A tropical cyclone (typhoon) impacts the upper atmosphere, ionosphere, and the magnetosphere via at least three channels, viz., acoustic–gravity, electromagnetic, and electrical ones, which are associated with the generation of waves and fields of the respective nature.
7. The schematic model presented above will be refined and improved in further research. However, it is already clear that satellite observations of variations in a number of atmospheric and geospace parameters are to expand the possibility of early warning of TCs (hurricanes, typhoons).
8. Observations of the ionospheric responses to a few unique typhoons made with the multifrequency multiple path software-defined radio system at oblique incidence verified the definitive role that IGWs and infrasound play in forming atmospheric–ionospheric disturbances. These observations have demonstrated that typhoon-induced disturbances can significantly affect the HF radio wave characteristics.
9. The Harbin Engineering University multifrequency multiple path coherent software-defined radio system for probing the ionosphere at oblique incidence was used to detect the ionospheric effects over the People's Republic of China during the 27 September 2018 to 13 October 2019 period encompassing the super typhoon event. The movement of the super typhoon was accompanied by significant variations in radio wave characteristics in the 5–10 MHz band.

The ionospheric effects are more pronounced along the nearest propagation paths, whereas no effect is detected along the propagation path at the greatest distance from the typhoon.

The super typhoon action on the ionosphere was accompanied by the generation or amplification of quasi-sinusoidal variations in the Doppler shift by a factor of 2–3, as well as by noticeable variations in the signal amplitude. The Doppler spectra were observed to broaden in a number of cases.

The period of wave perturbations exhibited variability in the ~20 min to ~120 min period range. This meant that the perturbations in the ionospheric electron density were caused by AGWs generated by the typhoon: the greater the AGW period, the greater the Doppler shift. As the period increased from 20 min to 120 min, the Doppler shift amplitudes increased from ~0.1 Hz to 0.5–1 Hz.

The most important mechanism of affecting the ionosphere has been confirmed to be associated with the generation of the 20–120 min period AGW by the typhoon, i.e., as the AGW period increases from 20 min to 60 min, the amplitude of quasi-sinusoidal variations in the electron density increases from 0.4 to 6 percent.

The Doppler measurements have shown that dusk terminators and the super typhoon acted synergistically to amplify the ionospheric response to these sources of energy.

Funding: L.F. Chernohor's research was conducted within the framework of the project of the National Research Foundation of Ukraine (project 2020.02/0015, "Theoretical and experimental studies of global disturbances from natural and technogenic sources in the Earth-atmosphere-ionosphere system"). This research was partially funded by Ukraine state-funded research projects #0121U109881 and #0122U001476.

Data Availability Statement: This paper is a review of the published literature.

Acknowledgments: The author thanks Victor T. Rozumenko at V. N. Karazin Kharkiv National University for helpful comments on some results and Yevhen H. Zhdanko at V. N. Karazin Kharkiv National University for assistance in compiling the manuscript.

Conflicts of Interest: The author declares no conflict of interest.

References

1. Chernogor, L.F. The tropical cyclone as an element of the Earth—Atmosphere—Ionosphere—Magnetosphere system. *Space Sci. Technol.* **2006**, *12*, 16–36. [CrossRef]
2. Chernogor, L.F. *On Nonlinearity in Nature and Science: Monograph*; V.N. Karazin Kharkiv National University Publ.: Kharkiv, Russia, 2008; 528p. (In Russian)
3. Chernogor, L.F. The Earth–atmosphere–geospace system: Main properties and processes. *Int. J. Remote Sens.* **2011**, *32*, 3199–3218. [CrossRef]
4. Chernogor, L.F.; Rozumenko, V.T. Earth—Atmosphere—Geospace as an Open Nonlinear Dynamical System. *Radio Phys. Radio Astron.* **2008**, *13*, 120–137. Available online: http://rpra-journal.org.ua/index.php/ra/article/view/563 (accessed on 7 October 2023).
5. Isaev, N.V.; Sorokin, V.M.; Chmyrev, V.M.; Serebryakova, O.N.; Yashchenko, A.K. Disturbance of the Electric Field in the Ionosphere by Sea Storms and Typhoons. *Cosm. Res.* **2002**, *40*, 547–553. [CrossRef]
6. Isaev, N.V.; Sorokin, V.M.; Chmyrev, V.M.; Serebryakova, O.N. Ionospheric electric fields related to sea storms and typhoons. *Geomagn. Aeron.* **2002**, *42*, 638–643.
7. Kuo, C.L.; Huba, J.D.; Joyce, G.; Lee, L.C. Ionosphere plasma bubbles and density variations induced by pre-earthquake rock currents and associated surface charges. *J. Geophys. Res.* **2011**, *116*, A10317. [CrossRef]
8. Yutsis, V.; Rapoport, Y.; Grimalsky, V.; Grytsai, A.; Ivchenko, V.; Petrishchevskii, S.; Fedorenko, A.; Krivodubskij, V. ULF Activity in the Earth Environment: Penetration of Electric Field from the Near-Ground Source to the Ionosphere under Different Configurations of the Geomagnetic Field. *Atmosphere* **2021**, *12*, 801. [CrossRef]
9. Yaroshevich, M.I.; Ingel, L.K. Tropical Cyclone: An Element of the Ocean-Atmosphere System. *Dokl. Earth Sci.* **2004**, *399*, 1245–1248. Available online: https://www.researchgate.net/publication/266535038_Tropical_cyclone_An_element_of_the_ocean-atmosphere_system (accessed on 7 October 2023).
10. Chernogor, L.F.; Garmash, K.P.; Guo, Q.; Rozumenko, V.T.; Zheng, Y.; Luo, Y. Supertyphoon Hagibis action in the ionosphere on 6–13 October 2019: Results from multi-frequency multiple path sounding at oblique incidence. *Adv. Space Res.* **2021**, *67*, 2439–2469. [CrossRef]
11. Chernogor, L.F.; Garmash, K.P.; Guo, Q.; Rozumenko, V.T.; Zheng, Y.; Luo, Y. Disturbances in the ionosphere that accompanied typhoon activity in the vicinity of China in September 2019. *Radio Sci.* **2022**, *57*, e2022RS007431. [CrossRef]
12. Zheng, Y.; Chernogor, L.F.; Garmash, K.P.; Guo, Q.; Rozumenko, V.T.; Luo, Y. Disturbances in the ionosphere and distortion of radio wave characteristics that accompanied the super typhoon Lekima event of 4–12 August 2019. *J. Geophys. Res.* **2022**, *127*, e2022JA030553. [CrossRef]
13. Chernogor, L.F.; Garmash, K.P.; Guo, Q.; Rozumenko, V.T.; Zheng, Y. Effects of the super-powerful tropospheric western Pacific phenomenon of September–October 2018 on the ionosphere over China: Results from oblique sounding. *Ann. Geophys.* **2023**, *41*, 173–195. [CrossRef]
14. Chernogor, L.F. Infrasound Effects of Earthquakes and Their Precursors on Parameters of Near-Earth Space. *Radio Phys. Radio Astron.* **1997**, *2*, 463–472. (In Russian)
15. Chernogor, L.F. Energetics of the Processes Occurring on the Earth, in the Atmosphere and Near-Earth Space in Connection with the Project "Early Warning". *Space Sci. Technol.* **1999**, *5*, 38–47. [CrossRef]
16. Chernogor, L.F. *Physics and Ecology of Disasters*; V. N. Karazin Kharkiv National University Publ.: Kharkiv, Russia, 2012; 556p. (In Russian)
17. Prasad, S.S.; Schneck, L.J.; Davies, K. Ionospheric disturbances by severe tropospheric weather storms. *J. Atmos. Terr. Phys.* **1975**, *37*, 1357–1363. [CrossRef]
18. Hung, R.J.; Kuo, J.P. Ionospheric observation of gravity-waves associated with Hurricane Eloise. *J. Geophys.* **1978**, *45*, 67–80. Available online: https://journal.geophysicsjournal.com/JofG/article/view/173 (accessed on 7 October 2023).
19. Krishnam Raju, D.G.; Rao, M.S.; Rao, B.M.; Jogulu, C.; Rao, C.P.; Ramanadham, R. Infrasonic oscillations in the F_2 region associated with severe thunderstorms. *J. Geophys. Res.* **1981**, *86*, 5873–5880. [CrossRef]
20. Boška, J.; Šauli, P. Observations of gravity waves of meteorological origin in the *F*-region ionosphere. *Phys. Chem. Earth* **2001**, *26*, 425–428. [CrossRef]
21. Chernigovskaya, M.A.; Shpynev, B.G.; Ratovsky, K.G. Meteorological effects of ionospheric disturbances from vertical radio sounding data. *J. Atmos. Solar-Terr. Phys.* **2015**, *136*, 235–243. [CrossRef]
22. Šindelářova, T.; Burešová, D.; Chum, J.; Hruška, F. Doppler observations of infrasonic waves of meteorological origin at ionospheric heights. *Adv. Space Res.* **2009**, *43*, 1644–1651. [CrossRef]
23. Hickey, M.P.; Schubert, G.; Walterscheid, R.L. Acoustic wave heating of the thermosphere. *J. Geophys. Res.* **2001**, *106*, 21543–21548. [CrossRef]
24. Hickey, M.P.; Walterscheid, R.L.; Schubert, G. Gravity wave heating and cooling of the thermosphere: Roles of the sensible heat flux and viscous flux of kinetic energy. *J. Geophys. Res.* **2011**, *116*, A12326. [CrossRef]
25. Gavrilov, N.M.; Kshevetskii, S.P. Dynamical and thermal effects of nonsteady nonlinear acoustic-gravity waves propagating from tropospheric sources to the upper atmosphere. *Adv. Space Res.* **2015**, *56*, 1833–1843. [CrossRef]

26. Karpov, I.V.; Kshevetskii, S.P. Numerical study of heating the upper atmosphere by acoustic-gravity waves from local source on the Earth's surface and influence of this heating on the wave propagation conditions. *J. Atmos. Solar-Terr. Phys.* **2017**, *164*, 89–96. [CrossRef]
27. Kuester, M.A.; Alexander, M.J.; Ray, E.A. A model study of gravity waves over Hurricane Humberto (2001). *J. Atmos. Sci.* **2008**, *65*, 3231–3246. [CrossRef]
28. Mikhailova, G.A.; Mikhailov, M.Y.; Kapustina, O.V. ULF–VLF electric fields in the external ionosphere over powerful typhoons in Pacific Ocean. *Int. J. Geomag. Aeron.* **2000**, *2*, 153–158. [CrossRef]
29. Mikhailova, G.A.; Mikhailov, Y.M.; Kapustina, O.V. Variations of ULF-VLF electric fields in the external ionosphere over powerful typhoons in Pacific Ocean. *Adv. Space Res.* **2002**, *30*, 2613–2618. [CrossRef]
30. Nickolaenko, A.P.; Hayakawa, M. Heating of the lower ionosphere electrons by electromagnetic radiation of lightning discharges. *Geophys. Res. Lett.* **1995**, *22*, 3015–3018. [CrossRef]
31. Bortnik, J.; Inan, U.S.; Bell, T.F. Temporal signatures of radiation belt electron precipitation induced by lightning-generated MR whistler waves: 1. Methodology. *J. Geophys. Res.* **2006**, *111*, A02204. [CrossRef]
32. Isaev, N.V.; Kostin, V.M.; Belyaev, G.G.; Ovcharenko, O.Y.; Trushkina, E.P. Disturbances of the topside ionosphere caused by typhoons. *Geomag. Aeron.* **2010**, *50*, 243–255. [CrossRef]
33. Sorokin, V.M.; Isaev, N.V.; Yaschenko, A.K.; Chmyrev, V.M.; Hayakawa, M. Strong DC electric field formation in the low latitude ionosphere over typhoons. *J. Atmos. Solar-Terr. Phys.* **2005**, *67*, 1269–1279. [CrossRef]
34. Sorokin, V.M.; Chmyrev, V.M.; Hayakawa, M. A Review on Electrodynamic Influence of Atmospheric Processes to the Ionosphere. *Open J. Earthq. Res.* **2020**, *9*, 113–141. [CrossRef]
35. Pulinets, S.; Davidenko, D. Ionospheric precursors of earthquakes and global electric circuit. *Adv. Space Res.* **2014**, *53*, 709–723. [CrossRef]
36. Okuzawa, T.; Shibata, T.; Ichinose, T.; Takagi, K.; Nagasawa, C.; Nagano, I.; Mambo, M.; Tsutsui, M.; Ogawa, T. Short-period disturbances in the ionosphere observed at the time of typhoons in September 1982 by a network of HF Doppler receivers. *J. Geomag. Geoelectr.* **1986**, *38*, 239–266. [CrossRef]
37. Xiao, Z.; Xiao, S.-G.; Hao, Y.-Q.; Zhang, D.-H. Morphological features of ionospheric response to typhoon. *J. Geophys. Res.* **2007**, *112*, A04304. [CrossRef]
38. Vanina–Dart, L.B.; Pokrovskaya, I.V.; Sharkov, E.A. Studying the interaction between the lower equatorial ionosphere and tropical cyclones according to data of remote and rocket sounding. *Izv. Atmos. Ocean. Phys.* **2007**, *2*, 19–27.
39. Afraimovich, E.L.; Voeykov, S.V.; Ishin, A.B.; Perevalova, N.P.; Ruzhin, Y.Y. Variations in the total electron content during the powerful typhoon of August 5–11, 2006, near the southeastern coast of China. *Geomag. Aeron.* **2008**, *48*, 674–679. [CrossRef]
40. Polyakova, A.S.; Perevalova, N.P. Investigation into impact of tropical cyclones on the ionosphere using GPS sounding and NCEP/NCAR reanalysis data. *Adv. Space Res.* **2011**, *48*, 1196–1210. [CrossRef]
41. Polyakova, A.S.; Perevalova, N.P. Comparative analysis of TEC disturbances over tropical cyclone zones in the north-west Pacific Ocean. *Adv. Space Res.* **2013**, *52*, 1416–1426. [CrossRef]
42. Zakharov, V.I.; Kunitsyn, V.E. Regional features of atmospheric manifestations of tropical cyclones according to ground-based GPS network data. *Geomagn. Aeron.* **2012**, *52*, 533–545. [CrossRef]
43. Zakharov, V.I.; Pilipenko, V.A.; Grushin, V.A.; Khamidullin, A.F. Impact of typhoon Vongfong 2014 on the Ionosphere and Geomagnetic Field According to Swarm Satellite Data: 1. Wave Disturbances of Ionospheric Plasma. *Solar-Terr. Phys.* **2019**, *5*, 101–108.
44. Zakharov, V.I.; Sigachev, P.K. Ionospheric disturbances from tropical cyclones. *Adv. Space Res.* **2022**, *69*, 132–141. [CrossRef]
45. Chou, M.Y.; Lin, C.C.H.; Yue, J.; Tsai, H.F.; Sun, Y.Y.; Liu, J.Y.; Chen, C.H. Concentric traveling ionosphere disturbances triggered by Super Typhoon Meranti (2016). *Geophys. Res. Let.* **2017**, *44*, 1219–1226. [CrossRef]
46. Chum, J.; Liu, J.-Y.; Šindelářová, K.; Podolská, T. Infrasound in the ionosphere from earthquakes and typhoons. *J. Atmos. Sol.–Terr. Phys.* **2018**, *171*, 72–82. [CrossRef]
47. Li, W.; Yue, J.; Yang, Y.; Li, Z.; Guo, J.; Pan, Y.; Zhang, K. Analysis of ionospheric disturbances associated with powerful cyclones in East Asia and North America. *J. Atmos. Solar-Terr. Phys.* **2017**, *161*, 43–54. [CrossRef]
48. Li, W.; Yue, J.; Wu, S.; Yang, Y.; Li, Z.; Bi, J.; Zhang, K. Ionospheric responses to typhoons in Australia during 2005–2014 using GNSS and FORMOSAT-3/COSMIC measurements. *GPS Solut.* **2018**, *22*, 61. [CrossRef]
49. Suzuki, S.; Vadas, S.L.; Shiokawa, K.; Otsuka, Y.; Karwamura, S.; Murayama, Y. Typoon-induced concentric airglow structures in the mesopause region. *Geophys. Res. Lett.* **2013**, *40*, 5983–5987. [CrossRef]
50. Yiğit, E.; Knížová, P.K.; Georgieva, K.; Ward, W. A review of vertical coupling in the Atmosphere–Ionosphere system: Effects of waves, sudden stratospheric warmings, space weather, and of solar activity. *J. Atmos. Solar-Terr. Phys.* **2016**, *141*, 1–12. [CrossRef]
51. Hocke, K.; Schlegel, K. A review of atmospheric gravity waves and travelling ionospheric disturbances: 1982-1995. *Ann. Geophys.* **1996**, *14*, 917–940. [CrossRef]
52. Kubota, M.; Shiokawa, K.; Ejiri, M.K.; Otsuka, Y.; Ogawa, T.; Sakanoi, T.; Fukunishi, H.; Yamamoto, M.; Fukao, S.; Saito, A. Traveling ionospheric disturbances observed in the OI 630-nm nightglow images over Japan by using a Multipoint Imager Network during the FRONT Campaign. *Geophys. Res. Lett.* **2000**, *27*, 4037–4040. [CrossRef]
53. Shiokawa, K.; Ihara, C.; Otsuka, Y.; Ogawa, T. Statistical study of nighttime medium-scale traveling ionospheric disturbances using midlatitude airglow images. *J. Geophys. Res.* **2003**, *108*, 1052. [CrossRef]

54. Fukushima, D.; Shiokawa, K.; Otsuka, Y.; Ogawa, T. Observation of equatorial nighttime medium-scale traveling ionospheric disturbances in 630-nm airglow images over 7 years. *J. Geophys. Res.* **2012**, *117*, A10324. [CrossRef]
55. Frissell, N.A.; Baker, J.B.H.; Ruohoniemi, J.M.; Gerrard, A.J.; Miller, E.S.; Marini, J.P.; West, M.L.; Bristow, W.A. Climatology of medium-scale traveling ionospheric disturbances observed by the midlatitude Blackstone SuperDARN radar. *J. Geophys. Res. Space Phys.* **2014**, *119*, 7679–7697. [CrossRef]
56. Paulino, I.; Medeiros, A.F.; Vadas, S.L.; Wrasse, C.M.; Takahashi, H.; Buriti, R.A.; Leite, D.; Filgueira, S.; Bageston, J.V.; Sobral, J.H.A.; et al. Periodic waves in the lower thermosphere observed by OI630 nm airglow images. *Ann. Geophys.* **2016**, *34*, 293–301. [CrossRef]
57. Paulino, I.; Moraes, J.F.; Maranhão, G.L.; Wrasse, C.M.; Buriti, R.A.; Medeiros, A.F.; Paulino, A.R.; Takahashi, H.; Makela, J.J.; Meriwether, J.W.; et al. Intrinsic parameters of periodic waves observed in the OI6300 airglow layer over the Brazilian equatorial region. *Ann. Geophys.* **2018**, *36*, 265–273. [CrossRef]
58. Song, Q.; Ding, F.; Zhang, X.; Liu, H.; Mao, T.; Zhao, X.; Wang, Y. Medium-scale traveling ionospheric disturbances induced by Typhoon Chan-hom over China. *J. Geophys. Res.* **2019**, *124*, 2223–2237. [CrossRef]
59. Zhao, Y.; Deng, Y.; Wang, J.-S.; Zhang, S.-R.; Lin, C.Y. Tropical cyclone-induced gravity wave perturbations in the upper atmosphere: GITM-R simulations. *J. Geophys. Res.* **2020**, *125*, e2019JA027675. [CrossRef]
60. Zhao, Y.X.; Mao, T.; Wang, J.S.; Chen, Z. The 2D features of tropical cyclone Usagi's effects on the ionospheric total electron content. *Adv. Space Res.* **2018**, *62*, 760–764. [CrossRef]
61. Wen, Y.; Jin, S. Traveling Ionospheric Disturbances Characteristics during the 2018 Typhoon Maria from GPS Observations. *Remote Sens.* **2020**, *12*, 746. [CrossRef]
62. Chen, J.; Zhang, X.; Ren, X.; Zhang, J.; Freeshah, M.; Zhao, Z. Ionospheric disturbances detected during a typhoon based on GNSS phase observations: A case study for typhoon Mangkhut over Hong Kong. *Adv. Space Res.* **2020**, *66*, 1743–1753. [CrossRef]
63. Freeshah, M.; Zhang, X.; Şentürk, E.; Adil, M.A.; Mousa, B.G.; Tariq, A.; Ren, X.; Refaat, M. Analysis of Atmospheric and Ionospheric Variations Due to Impacts of Super Typhoon Mangkhut (1822) in the Northwest Pacific Ocean. *Remote Sens.* **2021**, *13*, 661. [CrossRef]
64. Ke, F.Y.; Qi, X.M.; Wang, Y.; Liu, X.W. Statistics of ionospheric responses to Southeast Asia's typhoons during 2006-2018 using the rate of change in the TEC index. *Adv. Space Res.* **2020**, *66*, 1724–1742. [CrossRef]
65. Kong, J.; Yao, Y.; Xu, Y.; Kuo, C.; Zhang, L.; Liu, L.; Zhai, C. A clear link connecting the troposphere and ionosphere: Ionospheric reponses to the 2015 Typhoon Dujuan. *J. Geod.* **2017**, *91*, 1087–1097. [CrossRef]
66. Das, B.; Sarkar, S.; Haldar, P.K.; Midya, S.K.; Pal, S. *D*-region ionospheric disturbances associated with the Extremely Severe Cyclone Fani over North Indian Ocean as observed from two tropical VLF stations. *Adv. Space Res.* **2021**, *67*, 75–86. [CrossRef]
67. Gill, A.E. *Atmosphere-Ocean Dynamics*, 1st ed.; Academic Press: New York, NY, USA, 1982; 662p.
68. Golitsyn, G.S. Statistics and Energetics of Tropical Cyclones. *Dokl. Akad. Nauk* **1997**, *354*, 535–538. (In Russian)
69. Golitsyn, G.S.; Yaroshevich, M.I. Specific features of the recurrence of tropical cyclones versus their energy. *Dokl. Akad. Nauk* **2000**, *372*, 544–546. (In Russian)
70. Matveev, Y.L.; Matveev, L.T. Characteristic Features of the Formation, Development, and Motion of Tropical Cyclones. *Izv. Atmos. Ocean. Phys.* **2000**, *36*, 698–705. Available online: https://www.researchgate.net/publication/287447583_Characteristic_features_of_the_formation_development_and_motion_of_tropical_cyclones (accessed on 7 October 2023).
71. Khain, A.P.; Sutyrin, G.G. *Tropical Cyclones and Their Interaction with the Ocean*; Gidrometeoizdat: Leningrad, Russia, 1983; 272p. (In Russian)
72. Shuleikin, V.V. *Calculation of the Development, Motion, and Damping of Tropical Hurricanes and the Major Waves They Create*; Gidrometeoizdat: Leningrad, Russia, 1978; 97p. (In Russian)
73. Inan, U.; Piddyachiy, D.; Peter, W.; Sauvaud, J.; Parrot, M. DEMETER satellite observations of lightning-induced electron precipitation. *Geophys. Res. Lett.* **2007**, *34*, L07103. [CrossRef]
74. Voss, H.D.; Imhof, W.L.; Walt, M.; Mobilia, J.; Gaines, E.E.; Reagan, J.B.; Inan, U.S.; Helliwell, R.A.; Carpenter, D.L.; Katsufrakis, J.P.; et al. Lightning-induced electron precipitation. *Nature* **1984**, *312*, 740–742. [CrossRef]
75. Voss, H.D.; Walt, M.; Imhof, W.L.; Mobilia, J.; Inan, U.S. Satellite observations of lightning-induced electron precipitation. *J. Geophys. Res.* **1998**, *103*, 11725–11744. [CrossRef]
76. Gossard, E.E.; Hooke, W.H. *Waves in the Atmosphere: Atmospheric Infrasound and Gravity Waves, Their Generation and Propagation*; Elsevier Scientific Publ. Co.: Amsterdam, The Netherlands, 1975; 472p.
77. Grigor'ev, G.I. Acoustic-gravity waves in the earth's atmosphere (review). *Radiophys. Quantum Electron.* **1999**, *42*, 1–21. [CrossRef]
78. Drobyazko, I.N.; Krasil'nikov, V.N. Generation of acoustic-gravity waves by atmospheric turbulence. *Radiophys. Quantum Electron.* **1985**, *28*, 946–952. [CrossRef]
79. Yampolski, Y.M.; Zalizovski, A.V.; Litvinenko, L.M.; Lizunov, G.V.; Groves, K.; Moldwin, M. Magnetic Field Variations in Antarctica and the Conjugate Region (New England) Stimulated by Cyclone Activity. *Radio Phys. Radio Astron.* **2004**, *9*, 130–151. (In Russian)
80. Brekhovskikh, L.M. On the radiation of infrasound into the atmosphere by oceanic waves. *Izv. Akad. Nauk. SSSR* **1968**, *4*, 444–450. (In Russian)
81. Kshevetskii, S.P.; Gavrilov, N.M. Vertical propagation of nonlinear gravity waves and their breaking in the atmosphere. *Geomagn. Aeron.* **2003**, *43*, 69–76.

82. Fritts, D.C.; Lund, T.S. Gravity Wave Influences in the Thermosphere and Ionosphere: Observations and Recent Modeling. In *Aeronomy of the Earth's Atmosphere and Ionosphere*; Abdu, M., Pancheva, D., Eds.; IAGA Special Sopron Book Series; Springer: Dordrecht, The Netherlands, 2011. [CrossRef]
83. Lizunov, G.; Skorokhod, T.; Hayakawa, M.; Korepanov, V. Formation of Ionospheric Precursors of Earthquakes—Probable Mechanism and Its Substantiation. *Open J. Earthq. Res.* **2020**, *9*, 142–169. [CrossRef]
84. Holzworth, R.H.; Kelley, M.C.; Siefring, C.L.; Hale, L.C.; Mitchell, J.D. Electrical measurements in the atmosphere and the ionosphere over an active thunderstorm. 2. Direct current electric fields and conductivity. *J. Geophys. Res.* **1985**, *90*, 9824–9830. [CrossRef]
85. Chernogor, L.F. Physical effects of the January 15, 2022, powerful Tonga volcano explosion in the Earth-atmosphere-ionosphere-magnitosphere system. *Space Sci. Technol.* **2023**, *29*, 54–77. [CrossRef]
86. Sedunov, Y.S.; Avdiushin, S.I.; Borisenkov, E.P.; Volkovitsky, O.A.; Petrov, N.N.; Reitenbakh, R.G.; Smirnov, V.I.; Chernikov, A.A. (Eds.) *Atmosphere Handbook*; Gidrometeoizdat: Leningrad, Russia, 1991; p. 510. (In Russian)
87. Reist, P.C. *Introduction to Aerosol Science*; MacMillan Publ. Co.: New York, NY, USA, 1984; 299p.
88. Chalmers, J.A. *Atmospheric Electricity*, 2nd ed.; Pergamon Press: Oxford, UK, 1967; 526p, ISBN 9781483185965.
89. Bliokh, P. Variations of Electric Fields and Currents in the Lower Ionosphere Produced by Conductivity Growth of the Air above the Future Earthquake Center. In *Atmospheric and Ionospheric Electromagnetic Phenomena Associated with Earthquakes*; Hayakawa, M., Ed.; TERRAPUB: Tokyo, Japan, 1999; pp. 829–838.
90. Denisenko, V.; Pomozov, E. Penetration of an Electric Field from the Surface Layer of the Atmosphere into the Ionosphere. *Sol.-Terr. Phys.* **2010**, *16*, 70–75. (In Russian)
91. Denisenko, V.V.; Ampferer, M.; Pomozov, E.V.; Kitaev, A.V.; Hausleitner, W.; Stangl, G.; Biernat, H.K. On electric field penetration from ground into the ionosphere. *J. Atmos. Sol.-Terr. Phys.* **2013**, *102*, 341–353. [CrossRef]
92. Denisenko, V.V.; Nesterov, S.A.; Boudjada, M.Y.; Lammer, H. A mathematical model of quasistationary electric field penetration from ground to the ionosphere with inclined magnetic field. *J. Atmos. Sol.-Terr. Phys.* **2018**, *179*, 527–537. [CrossRef]
93. Denisenko, V.V.; Boudjada, M.Y.; Horn, M.; Pomozov, E.V.; Biernat, H.K.; Schwingenschuh, K.; Lammer, H.; Prattes, G.; Cristea, E. Ionospheric conductivity effects on electrostatic field penetration into the ionosphere. *Nat. Hazards Earth Syst. Sci.* **2008**, *8*, 1009–1017. [CrossRef]
94. Marshall, R.A. An improved model of the lightning electromagnetic field interaction with the D-region ionosphere. *J. Geophys. Res.* **2012**, *117*, A03316. [CrossRef]
95. Gordillo-Vázquez, F.J.; Luque, A.; Haldoupis, C. Upper D region chemical kinetic modeling of LORE relaxation times. *J. Geophys. Res. Space Phys.* **2016**, *121*, 3525–3544. [CrossRef]
96. Barta, V.; Haldoupis, C.; Sátori, G.; Buresova, D.; Chum, J.; Pozoga, M.; Berényi, K.A.; Bór, J.; Popek, M.; Kis, Á.; et al. Searching for effects caused by thunderstorms in midlatitude sporadic E layers. *J. Atmos. Sol.-Terr. Phys.* **2017**, *161*, 150–159. [CrossRef]
97. Kelley, M.C.; Siefring, C.L.; Pfaff, R.P.; Kintner, P.M.; Larsen, M.; Green, R.; Holzworth, R.H.; Hale, L.C.; Mitchell, J.D.; Le Vine, D. Electrical measurements in the atmosphere and the ionosphere over an active thunderstorm. 1. Campaign overview and initial ionospheric results. *J. Geophys. Res.* **1985**, *90*, 9815–9823. [CrossRef]
98. Kraus, E.B.; Businger, J.A. *Atmosphere-Ocean Interaction*, 2nd ed.; Oxford University Press, Inc.: New York, NY, USA, 1994; 362p.
99. Trakhtengerts, V.Y.; Rycroft, M.J. *Whistler and Alfvén Mode Cyclotron Masers in Space*; Cambridge University Press: Cambridge, UK, 2010; 354p. [CrossRef]